



HAL
open science

Quantitative assessments of moisture sources and temperature governing rainfall $\delta^{18}\text{O}$ from 20 years' monitoring records in SW-France: Importance for isotopic-based climate reconstructions

Jian Zhang, Dominique Genty, Colette Sirieix, Simon Michel, Bénédicte Minster, Édouard Régner

► To cite this version:

Jian Zhang, Dominique Genty, Colette Sirieix, Simon Michel, Bénédicte Minster, et al.. Quantitative assessments of moisture sources and temperature governing rainfall $\delta^{18}\text{O}$ from 20 years' monitoring records in SW-France: Importance for isotopic-based climate reconstructions. *Journal of Hydrology*, 2020, 591, pp.125327. 10.1016/j.jhydrol.2020.125327 . hal-02970833

HAL Id: hal-02970833

<https://hal.science/hal-02970833>

Submitted on 22 Aug 2022

HAL is a multi-disciplinary open access archive for the deposit and dissemination of scientific research documents, whether they are published or not. The documents may come from teaching and research institutions in France or abroad, or from public or private research centers.

L'archive ouverte pluridisciplinaire **HAL**, est destinée au dépôt et à la diffusion de documents scientifiques de niveau recherche, publiés ou non, émanant des établissements d'enseignement et de recherche français ou étrangers, des laboratoires publics ou privés.



Distributed under a Creative Commons Attribution - NonCommercial 4.0 International License

1 **Quantitative assessment of moisture source and temperature**
2 **governing rainfall $\delta^{18}\text{O}$ from 20 years long monitoring records in**
3 **SW-France: Importance for isotopic-based climate reconstructions**

4 Jian Zhang ^{a, b*}, Dominique Genty ^{a*}, Colette Sirieix ^b, Simon Michel ^a, Bénédicte
5 Minster ^c, Edouard Régnier ^c

6 ^a *Environnements et Paléoenvironnements Océaniques et Continentaux (EPOC),*
7 *UMR CNRS, 5805, Université de Bordeaux, 33615 Pessac Cedex, France*

8 ^b *CNRS, Arts et Metiers Institute of Technology, Bordeaux INP, INRAE, I2M*
9 *Bordeaux, Université de Bordeaux, 33400 Talence, France*

10 ^c *Laboratoire de Sciences du Climat et de l'Environnement (LSCE), Orme des*
11 *Merisiers, UMR 8212 CEA/CNRS/UVSQ, 91191 Gif-sur-Yvette Cedex, France*

12

13

14 **Submitted the minor revised version to Journal of hydrology**

15

16

17

18 First author: Jian Zhang

19 * The corresponding author: Jian Zhang and Dominique Genty

20 E-mail: jian.zhang@u-bordeaux.fr and dominique.genty@u-bordeaux.fr

21 Postal Address: Allée Geoffroy Saint-Hilaire Bât. NB18, Université de Bordeaux,
22 Pessac, France

23 **Abstract**

24 In the mid-high latitude region, variations of stable isotopic compositions of
25 atmospheric precipitation ($\delta^{18}\text{O}_p$ and δD_p) were commonly regarded as reflecting a
26 “temperature effect”. However, some studies have indicated that the change of
27 moisture source was an important controlling factor for $\delta^{18}\text{O}_p$. To clarify whether
28 there is connection between $\delta^{18}\text{O}_p$ and the variation of moisture source in Southwest
29 France (SW-France), whose implication for speleothem paleoclimatic interpretation is
30 of great importance, we have used among the longest isotopic time series from
31 SW-France (Le Mas and Villars stations) and a 5 days’ reconstruction of air mass
32 history during the 1997-2016 A.D period based on HYSPLIT tracking model. We
33 found the percentage of initial moisture sources (PIMS) as an important factor
34 controlling the oxygen isotope composition of precipitation in SW-France, whether
35 monthly or inter-annual timescales was considered. Additionally, we found that the
36 $\delta^{18}\text{O}_p$ preserved the signal of local temperature, supporting a “temperature effect”,
37 while no evidence for its “amount effect” have been observed. These quantified links
38 between PIMS/local-temperature and $\delta^{18}\text{O}_p$ appears useful to better understand the
39 links between stable oxygen isotopes and climate parameters. Our long-term
40 monitoring of the $\delta^{18}\text{O}_p$, d-excess, and moisture sources reveals decadal trends,
41 highlighting a tight coupling in hydrologic systems and relatively fast changes in
42 SW-France rainfall sources controlled by atmospheric circulations.

43 **Keywords:** Rainfall; Isotope ratios; HYSPLIT model; Moisture Sources;
44 Temperature; Southwest France

45 **Main manuscript content**

46 **1. Introduction**

47 The stable isotopic compositions of atmospheric precipitation ($\delta^{18}\text{O}_p$ and δD_p)
48 (See acronyms in Appendix Table 1) are important tools for understanding regional
49 atmospheric circulation and local hydrological cycle (Dansgaard, 1964; Sharp, 2007;
50 Gat, 2010; Genty et al., 2014). The mechanism between the temperature/precipitation
51 and isotope ratios in rainfall are considerably complex, including these processes like
52 Rayleigh fractionation, diffusive exchange of isotopes between raindrops and vapor,
53 as well as re-evaporation of falling rainfall (Fricke and O'Neil, 1999;
54 Araguás-Araguás et al., 2000, 2005; Risi et al., 2008; Lachniet, 2009; Field et al.,
55 2010). The $\delta^{18}\text{O}$ in many natural archives has been used to reconstruct the
56 paleoenvironment over the past few years (Pettit et al., 1999; Wang et al., 2001; Hu et
57 al., 2008; Zhang et al., 2008; McDermott et al., 2011). Thus, the investigation and
58 qualification on the various factors governing the rainfall stable isotopes are of great
59 importance for the paleoclimate community (Krklec and Domínguez-Villar., 2014;
60 Krklec et al., 2018).

61 Average monthly local temperatures, generally measured 2 m above ground
62 level, are statistically correlated with the monthly $\delta^{18}\text{O}_p$ and δD_p on middle and
63 high-latitude monitoring stations, called “temperature effect” (Dansgaard, 1964;
64 IAEA working group, 2000), particularly obvious on the European continent (Krklec
65 and Domínguez-Villar, 2014; Krklec et al., 2018), however, the relationship on the
66 inter-annual timescale remains unclear. Additionally, some researchers have revealed
67 that the inter-annual atmospheric variability, such as North Atlantic Oscillation
68 (NAO), also controls the rainfall isotopic value (Baldini et al., 2008;
69 Fischer and Matthey, 2012). However, local precipitation amount and monthly isotope
70 ratios do not exhibit significant correlations in continental Europe (Dansgaard, 1964).

71 Some previous studies have proposed that the moisture source was an important
72 controlling factor for $\delta^{18}\text{O}_p$ and δD_p (Cruz et al., 1992; Cole et al., 1999; Friedman et
73 al., 2002; Lachniet, 2009). Moisture source location is generally estimated by the
74 calculation of the deuterium excess (d-excess), which is significantly different
75 between the Atlantic Ocean and the Mediterranean Sea (Dansgaard, 1964; Craig and
76 Gordon, 1965; Vimeux et al., 1999; Uemura et al., 2012). Moreover, d-excess also
77 reflect the variation on near-surface relative humidity (RH) during evaporation and
78 moisture source temperature variations (Pfahal and Sodemann, 2014). However, by
79 using this method, it is extremely difficult to quantify the pathway of water vapor
80 transportation, limiting the understanding of the change of moisture source for $\delta^{18}\text{O}_p$
81 and δD_p , particularly for spatial and temporal evapotranspiration (ET) contributions.

82 To overcome this issue, the history of air masses have been calculated by
83 studying regional/general circulation using Lagrangian models. However, obvious
84 discrepancies between observed isotopes and the variation of modeled air masses
85 were questioned, which may be due to insufficient accuracy of the models (Hoffmann
86 et al., 1998; Sturm, 2005; Schmidt et al., 2007; Sodemann et al., 2008; Pfahl and
87 Wernli, 2008; Langebroek et al., 2011). Therefore, this raised question of how to
88 accurately quantify the variability of initial moisture sources, which are important for
89 explaining the climatic significance of $\delta^{18}\text{O}_p$ and δD_p (Aggarwal et al., 2004; Dayem
90 et al., 2010; Domínguez-Villar et al., 2017).

91 The Hybrid Single-Particle Lagrangian Integrated Trajectory (HYSPLIT)
92 model (Draxler and Hess, 1998), an advanced system calculating air parcel
93 trajectories, has been greatly promoted (Stein et al., 2015). This atmospheric
94 calculation model based on the Eulerian and hybrid Lagrangian approaches can
95 accurately reflect the variation of moisture source (Stein et al., 2015). Among them,
96 the Lagrangian method is using a moving framework as references for the calculations
97 of diffusion and advection when the trajectories or air parcels move from initial
98 source region, and the Eulerian methodology is using a restricted three-dimensional
99 grid cell to compute air concentrations (Stein et al., 2015). Additionally, HYSPLIT
100 software has been successfully applied in several studies including tracking the
101 atmospheric circulation change (Sjostrom and Welker, 2009; Breitenbach et al., 2010;
102 Abouelmagd et al., 2012; Dumitru et al., 2017; Sánchez - Murillo et al., 2020),

103 predicting the direction of pollutant diffusion (Chen et al., 2012) and monitoring
104 wildfire smoke (Rolph et al. 2009).

105 In Southwest France (SW-France), there are very few published data concerning
106 stable isotopes of precipitation, especially for long time-series (i.e. > 10 years). Our
107 research sites, including Le Mas and Villars stations, are situated on karst areas, and
108 rainfall isotope ratios (e.g. $\delta^{18}\text{O}_p/\delta\text{D}_p$) are regarded as a good tool to determine the
109 sources of the seepage water (Ladouche et al., 2009) and its variations in time and
110 consequences on isotopic cave calcite composition (speleothems) (Genty et al., 2001,
111 2006, 2014; Genty, 2008). More importantly, this area is a key place for studying the
112 moisture pathways from the North Atlantic and the Mediterranean across the
113 European continent (Duffourg and Ducrocq, 2011), and our long-term observations
114 for the rainfall $\delta^{18}\text{O}_p$ as well as its environment parameters allow us to confidential
115 understand the local hydrological cycle and climate change.

116 In summary, there are the following unresolved scientific limitations about the
117 stable isotopic composition of the rainfall in SW-France, including: (1) unclear
118 relationships and mechanisms between initial moisture sources and $\delta^{18}\text{O}_p$ on the
119 monthly and inter-annual timescales. (2) unquantified links between $\delta^{18}\text{O}_p$ and various
120 controlling factors (temperature, rainfall and moisture source). Here, we combined
121 with $\delta^{18}\text{O}_p$ in SW-France, the data of moisture sources and regional/local climatic
122 parameters, addressing these above-mentioned scientific questions. Our study
123 attempts to determine the variation of initial moisture sources and its relation to the

124 stable isotopic composition of the rainfall in the SW-France using the HYSPLIT
125 model. The link between $\delta^{18}\text{O}_p$ and various controlling factors was also quantified to
126 eventually calibrate the link between local climate parameters and $\delta^{18}\text{O}_p$ as well as
127 deepen understanding for the significance of cave speleothem $\delta^{18}\text{O}$.

128 **2. Study area**

129 Rainfall samples were collected from two monitoring sites, namely Le Mas
130 (45°7'45"N, 1°11'31"E) and Villars (45°26'18"N, 0°47'2"E) (Figs. 1A and B) about
131 20 km far each other. During the monitoring period from 1997-2016, the mean annual
132 amount of precipitation at the Villars station is 1003 mm (Standard Deviation:150
133 mm), and the mean annual temperature is 12.5 °C. The region is composed of
134 limestone characterized by numerous carbonate caves, among them, Villars Cave was
135 extensively studied for its speleothems and cave environment (Genty et al., 2003,
136 2006, 2010, 2014; Genty, 2008).

137 The large-scale atmospheric circulation in Western Europe (WE) is affected by
138 climatic system influences from different geographic area, such as Atlantic,
139 Mediterranean, Greenland and European Continents (Giuntoli et al., 2013). The most
140 important circulation pattern is considered to be the winter North Atlantic Oscillation
141 (NAO) which is a driver for streamflow in North and West Europe (Trigo et al., 2002).
142 Other large-scale circulation patterns, such as the Arctic Oscillation (AO) or Atlantic

143 Multidecadal Oscillation (AMO) have also influenced the climatic variation in West
144 Europe region (O'Reilly et al., 2016).

145 In order to better quantify the spatial distribution of initial moisture source, the
146 research region was divided into six sections (Fig. 1A; Appendix Table 1), namely
147 Proximal Atlantic and West Europe (PAWE), Distal Atlantic (DA), North Atlantic
148 (NA), North America and Greenland (NAGR), Mediterranean (ME), Northern
149 European and Northern Atlantic (NENA) (referred and modified from Krklec and
150 Domínguez-Villar, 2014). These different regions have been defined on the basis of
151 European geographical limitations (e.g. ocean-continent borders and ocean boundary)
152 and distribution patterns of the initial seawater isotopic composition as well as the
153 concentrated locations of moisture sources (Fig. 1A; Lachniet, 2009; Krklec and
154 Domínguez-Villar, 2014).

155 **3. Methods and data**

156 **3.1 Stable isotopic composition of rainwater**

157 The stable isotopic samples were collected in the Le Mas and Villars stations at
158 an approximately monthly scale during the period from 1997 to 2016. Rainfall
159 sampling protocol follows the recommended principles from Global Network of
160 Isotope in Precipitation (GNIP) from the International Atomic Energy Agency
161 (IAEA). The rainwater is collected in a 5 L tank with a funnel. Before the tank is
162 buried in the soil, each sample have added a few ml of liquid paraffin to prevent any

163 evaporation. Water is collected into a 15 ml glass bottle which is closed by a specific
164 cork with a conical funnel making sure waterproofness.

165 The hydrogen isotopic composition (δD) of the precipitation sample was
166 measured on an ISO-PRIME mass spectrometer and a PICARRO laser spectrometer,
167 and the analytical absolute error for δD is $\pm 0.5\text{‰}$. The oxygen isotopes ($\delta^{18}O$) were
168 measured on a Finnigan MAT 252 by equilibration with CO_2 , with an analytical error
169 of $\pm 0.05\text{‰}$. In order to avoid potential paraffin pollution, all measured samples were
170 filtered through $0.2\mu m$ Anlypore filters. On the PICARRO spectrometer, the memory
171 effect was treated by doing 6 to 7 times' successive measurements of the same
172 sample, and by keeping only the last 3 results to determine the value of rainfall δD .
173 For the calibration, we used an internal EPB standard (Laboratoire de Sciences du
174 Climat et de l'Environnement: LSCE) as working reference standards that was
175 cross-checked. The final result of $\delta^{18}O$ and δD are then expressed relative to the
176 Vienna Standard Mean Ocean Water (V-SMOW). Early measurements in 1997 and
177 1998 were measured on a VG SIRA IRMS with an error of $\pm 0.2\text{‰}$ for the $\delta^{18}O$ while
178 δD was performed using the zinc reduction method with an error close to $\pm 2\text{‰}$ (Genty
179 [et al., 2014](#)).

180 **3.2 Meteorological data**

181 European precipitation data was downloaded from the Global Precipitation
182 Climatology Project (GPCP) Version 2.3 combining observations and satellite pr

183 ecipitation data with $2.5^{\circ}\times 2.5^{\circ}$ global grids (Website: <https://www.esrl.noaa.gov/psd>
184 [/data/gridded/data.gpcp.html](https://www.esrl.noaa.gov/psd/data/gridded/data.gpcp.html)). The air temperature data were obtained from the J
185 ones CRU Air Temperature Anomalies Version 4 with $5^{\circ}\times 5^{\circ}$ global grids (Webs
186 ite: <https://www.esrl.noaa.gov/psd/data/gridded/data.crutem4.html>). The sea surface
187 temperature (SST) data were obtained from Kaplan Extended SST Version 2
188 with $5^{\circ}\times 5^{\circ}$ global grids (https://psl.noaa.gov/data/gridded/data.kaplan_sst.html). Th
189 e NAO index was downloaded from the following official websites: [https://ww
190 w.ncdc.noaa.gov/teleconnections/nao/data.csv](https://www.ncdc.noaa.gov/teleconnections/nao/data.csv).

191 **3.3 HYSPLIT model for tracking moisture source**

192 To diagnose the moisture transportation pathways and better understand the
193 $\delta^{18}\text{O}_p$ variability in SW-France, we employed the method of back trajectories of air
194 parcels from the NCEP reanalysis data (Website:
195 <ftp://arlftp.arlhq.noaa.gov/pub/archives/reanalysis>). The HYSPLIT model was
196 downloaded from the NOAA Air Resources Laboratory (Website:
197 <http://ready.arl.noaa.gov/HYSPLIT.php>) (Draxler and Rolph, 2010). In order to
198 analyze the temporal variability of moisture sources, we have divided a year into four
199 seasons: spring (March–May), summer (June–August), autumn (September–
200 November), and winter (December–February of the following year).

201 Previous studies have revealed that trajectories with the average residence time
202 of water vapor in the atmosphere are 120 hours (5 days) (Numaguti, 1999; Krklec and
203 Domínguez-Villar, 2014). Therefore, the variation of moisture sources were identified

204 in the Villars station (we assumed a common source for Le Mas station being very
205 close to Villars) during the previous 120 h (5 days) (Krklec and Domínguez-Villar,
206 2014; Krklec et al., 2018). The water vapor transportation usually occurs mainly at
207 1500m-3000m (above ground level: a.g.l) in the mid-low troposphere, however, the
208 peak value of water vapor transportation in the plain is an at altitude of about 1500 m
209 (~ 850 hPa) (Tang et al., 2015; Cai et al., 2017). Moreover, the back trajectories from
210 different elevations showed similar paths and regulations (Krklec and
211 Domínguez-Villar, 2014; Krklec et al., 2018), therefore we consider the only altitude
212 of 1500 m (a.g.l) as the initial vertical height for the water vapor transportation.

213 The integrated system was operated for computing the daily trajectory at the
214 time of 00:00, 06:00, 12:00 and 18:00, and the output of trajectories are made every 6
215 hours. The cluster analysis tool was applied for integrating all trajectories, which were
216 grouped according to the horizontal moving speed and direction in HYSPLIT model
217 (Tang et al., 2015). Finally, HYSPLIT4 software is used for superposition analysis
218 and designed to get the diagram to determine the variation of the initial moisture
219 source.

220 **3.4 Statistical methods and packages**

221 The correlations between regional parameters and $\delta^{18}\text{O}_p$ variability in
222 SW-France were calculated using R programming. Significance levels for correlations
223 were calculated using Student t-tests. Degrees of freedom corrections were calculated
224 by time-series autocorrelations (McCarthy et al., 2015):

$$225 \text{Neff} = N * ((1 - ax * ay) / (1 + ax * ay))$$

226 where Neff is the corrected degrees of freedom of Student t statistics, N is the
227 length of the time series, and ax, ay are the first order autocorrelation of each
228 time-series.

229 The links between PIMS/temperature and $\delta^{18}\text{O}_p$ were established using multiple
230 linear regression analysis methods by Statistical Package for the Social Sciences
231 (SPSS) software:

$$232 y_i = \beta_0 + \beta_1 x_{i1} + \beta_2 x_{i2} + \dots + \beta_p x_{ip} + \epsilon$$

233 where, for i denotes n factors; y_i denotes dependent variable; x_i denotes
234 explanatory variables; β_0 denotes y-intercept; β_p denotes
235 slope coefficients for each explanatory variable; ϵ denotes residuals.

236 4. Results

237 4.1 Relationship between $\delta^{18}\text{O}_p$ and local/regional climate parameters

238 The correlation of the $\delta^{18}\text{O}_p$ between Villars and Le Mas stations is 0.72 ($p < 0.01$)
239 (Figs. 2A, 2B), suggesting that both were controlled by the same air masse and
240 climate. Local meteoric water line (LMWL) in the two monitoring sites are defined by:
241 $\delta\text{D}_p = 6.91 * \delta^{18}\text{O}_p + 3.02$ ($p < 0.01$) for Le Mas and $\delta\text{D}_p = 7.08 * \delta^{18}\text{O}_p + 5.03$ ($p < 0.01$) for
242 Villars based on the linear regression (Fig. 2C). In order to verify the reliability of
243 LMWL equation, we also used other different methods, including ordinary least
244 squares regression (OLSR) and precipitation weighted least squares regression
245 (PWLSR) (Hughes and Crawford, 2012; Crawford et al., 2014). Whether weighted or
246 non-weighted regression was considered, close slope and gradient values were
247 observed from three methods (Table. 1). Rainfall stable isotopes are characterized by
248 strong seasonal variations with depleted average values in winter months (December,
249 January, February: -43.2‰ to -47.7‰ for δD_p and -6.9‰ to -7.5‰ for $\delta^{18}\text{O}_p$) and
250 enriched average values during summer months (June, July, August: -27.8‰ to -31.5‰
251 for δD_p and -4.6‰ to -5.1‰ for $\delta^{18}\text{O}_p$) (Appendix Table 2) in Villars and Le Mas
252 stations.

253 On a monthly timescale, $\delta^{18}\text{O}_p$ and local temperature show a positive correlation
254 at Villars ($R=0.61$, $p < 0.0001$) and Le Mas ($R=0.62$, $p < 0.0001$) for the considered
255 period (1996-2016) (Fig. 3A) with a T - $\delta^{18}\text{O}_p$ gradient of $0.17\text{‰}/^\circ\text{C}$ and $0.15\text{‰}/^\circ\text{C}$

256 respectively. This indicates that the $\delta^{18}\text{O}_p$ in SW-France is mainly affected by local
257 temperature. Compared with observed (Fricke and O'Neill, 1999; Alley and Cuffey,
258 2001) and modelled (Jouzel et al., 1997; Schmidt et al., 2007) T- $\delta^{18}\text{O}_p$ gradient over
259 the global-scale, ranging from 0.17‰/°C to 0.9‰/°C, the T- $\delta^{18}\text{O}_p$ gradient in the Le
260 Mas and Villars stations are close to the lowest values. On the contrary, $\delta^{18}\text{O}_p$ and
261 local precipitation do not exhibit a significant correlation: R=0.19 at Le Mas and
262 R=0.29 at Villars, with a gradient of -0.7‰/100mm and -0.8‰/100mm, respectively
263 (Fig. 3B).

264 In order to assess local $\delta^{18}\text{O}_p$ records in SW-France whether or not can be
265 sensitive to regional parameters variations, correlations between $\delta^{18}\text{O}_p$ from Le Mas
266 and Villars stations and European temperatures with 5°x5° global grids were
267 calculated on the seasonal timescale for the 1996-2016 period. Results show that
268 significant correlations are mostly found for winter (DJF) and spring (MAM) (Figs.
269 4A, 4B, 4E, 4F). At Le Mas station, the time-series of $\delta^{18}\text{O}_p$ displays positive
270 correlation with Northern Europe temperatures and negative ones with the
271 temperature of South Europe and Mediterranean area (Fig. 4A). A similar pattern also
272 occurs for the Villars station, although these correlations are weaker (Fig. 4E)
273 possibly due to a lack of some monthly data in Villars (Fig. 4E; Appendix data).
274 Moreover, during spring (MAM), the correlation of $\delta^{18}\text{O}_p$ and regional temperature
275 shows positive (Northwest Europe) and negative (North Africa and Mediterranean
276 area) relationships at both stations (Figs. 4B and 4F). Unlike the high correlation

277 between local temperature and $\delta^{18}\text{O}_p$ on all months, this regional relationship is only
278 reflected in winter and spring (Fig. 3A and Fig. 4).

279 The relationship between regional precipitation and $\delta^{18}\text{O}_p$ for all the seasons was
280 also considered (Fig. 5). Despite the globally much weaker correlations, we observe
281 that, in winter, regional precipitation with $2.5^\circ \times 2.5^\circ$ global grids and $\delta^{18}\text{O}_p$ shows a
282 similar spatial pattern between regional temperature and $\delta^{18}\text{O}_p$ (Figs. 4A, 4E, 5A, 5E).
283 During spring (MAM), the link between $\delta^{18}\text{O}_p$ and regional precipitation shows a
284 positive pattern with North Europe and North African and Mediterranean Sea and a
285 negative one all over the European continent (Figs. 5B and 5F). During summer (JJA)
286 and autumn (SON) seasons, no or less significant correlations were observed between
287 temperature/precipitation and $\delta^{18}\text{O}_p$ for both stations (Figs. 4C, 4D, 4G, 4H, 5C, 5D,
288 5G, 5H). The degrees of freedom corrections were calculated between the two 20-year
289 time-series of $\delta^{18}\text{O}_p$ from SW-France (Le Mas and Villars) and the Atlantic SST with
290 $5^\circ \times 5^\circ$ global grids (Fig. 6). The results show that $\delta^{18}\text{O}_p$ values are positively
291 correlated with SST in the Gulf Stream of Mexico (Figs. 6B, 6F), and opposite to SST
292 in northern and southern of North Atlantic, inducing a tripolar SST distribution in the
293 North Atlantic in spring. However, during other seasons, no or less significant
294 correlations were observed between SST and $\delta^{18}\text{O}_p$ for both stations (Figs. 6A, 6C,
295 6D, 6E, 6G, 6H).

296 Note that whether we consider the pattern of $\delta^{18}\text{O}_p$ and European temperature or
297 precipitation in Le Mas and Villars stations in winter and spring, it is similar to the

298 spatial pattern between NAO phase and European temperature and precipitation
299 (Cassou et al., 2004; Baldini et al., 2008; Figs. 4A, 4E, 5A, 5E). The link between
300 NAO index and $\delta^{18}\text{O}_p$ seems to be confirmed by their high correlation ($p < 0.01$ or
301 $p < 0.05$) in winter ($R = 0.45$ and $R = 0.42$) and spring ($R = 0.33$ and $R = 0.36$) (Figs. 7A, 7B,
302 7C, 7D).

303 **4.2 Relationship between $\delta^{18}\text{O}_p$ and initial moisture source on a** 304 **monthly timescale**

305 In order to localize the moisture sources of the rainfall (the percentage of initial
306 moisture, PIMS) that occur above Villars station, we first used the HYSPLIT software
307 for periods of high (summer) and low (winter) $\delta^{18}\text{O}_p$ (Fig. 8). Results show a clear
308 seasonal variability in the back trajectories with a much longer pathway in December,
309 January and February compared to the summer months (June, July and August) (Fig.
310 8). During winter, some vapor sources reach areas clearly beyond the 60° W meridian,
311 while in summer the extreme west source is significantly closer to Villars, around the
312 extreme east of Canada (Figs. 8D, 8E, 8F). But when replaced in the spatial pattern of
313 Figure 1, and looking at the actual percentages given by the software calculation
314 (Table 2), then it appears that water vapor source in winter is mostly distributed in the
315 region of NAGR (West North Atlantic: North America and Greenland) characterized
316 by a longer transportation (Table 2; Figs. 8A, 8B, 8C), while, in summer, it is mostly
317 from the closest source (PAWE: Proximal Atlantic and West Europe) (Table 2; Figs.
318 8D, 8E, 8F).

319 These results show that the sources (characterized by the PIMS) and rainfall
320 $\delta^{18}\text{O}_p$ in SW-France are characterized by a well-marked seasonality: negative $\delta^{18}\text{O}_p$
321 excursions occur in winter when there is the longer initial moisture location (e.g.
322 NAGR) (Table 2; Figs. 8A, 8B, 8C). On the contrary, the $\delta^{18}\text{O}_p$ in summer shows a
323 positive $\delta^{18}\text{O}_p$ excursion, which coincides with the closer initial moisture location (e.g.
324 PAWE) (Table 2; Figs. 8D, 8E, 8F).

325 During spring and autumn, there is no obvious contrasted PIMS (Fig. 9). We note
326 however that PIMS in the near summer months (e.g. May and September) is derived
327 from the increased closer moisture source (PAWE), and decreased longer moisture
328 source (NAGR), corresponding to heavier values of $\delta^{18}\text{O}_p$ and δD_p (Table 2 and
329 Appendix Table 2; Figs. 9C, 9D). In contrast, in the near winter months (e.g. March
330 and November), PIMS from the closer source (e.g. PAWE) is decreased, and longer
331 sources is increased (e.g. NAGR) (Table 2; Figs. 9A, 9F), which indicates that the
332 change of PIMS can regulate the $\delta^{18}\text{O}_p$ on the monthly timescale in SW-France.

333 These results highlight the close relationships between PIMS and $\delta^{18}\text{O}_p$ values at
334 Villars (and Le Mas). A high PIMS from closer regions (e.g. PAWE and NA) is
335 related to heavier $\delta^{18}\text{O}_p$ values while high PIMS from farther regions (e.g. NAGR) is
336 related to lower $\delta^{18}\text{O}_p$ values (Table 2; Appendix Table 2). Linear equations have
337 been established, for Le Mas and Villars stations, to quantify the relationship between
338 $\delta^{18}\text{O}_p$ and PIMS (Table 3). Results show a positive relationship ($p < 0.01$ or $p < 0.05$)
339 between $\delta^{18}\text{O}_p$ and PIMS in the region of PAWE and NA, and a negative relationship

340 ($p < 0.01$) between $\delta^{18}\text{O}_p$ and PIMS in the region of NAGR, whereas the rest of the
341 regions (ME and DA) have much less impact on $\delta^{18}\text{O}_p$ values (Table 3).

342 **4.3 Relationship between $\delta^{18}\text{O}_p$, d-excess and initial moisture** 343 **source/local climate parameters on the annual and inter-annual** 344 **timescale**

345 On the annual timescale, a positive relationship ($p < 0.05$), in both Le Mas and
346 Villars stations, is observed between the annual average $\delta^{18}\text{O}_p$ ($\delta^{18}\text{O}_{ap}$) and annual
347 mean temperature, with a T - $\delta^{18}\text{O}_{ap}$ gradient of $0.42\text{‰}/^\circ\text{C}$ and $0.51\text{‰}/^\circ\text{C}$, respectively.
348 These values fall in the range of gradients observed from global continental, marine
349 and polar sites ($0.17\text{‰}/^\circ\text{C}$ to $0.9\text{‰}/^\circ\text{C}$; Clark and Fritz, 1999; Figs. 10A, 10B). At the
350 opposite, P - $\delta^{18}\text{O}_{ap}$ gradients are low: $-0.1\text{‰}/100\text{mm}$ and $-0.07\text{‰}/100\text{mm}$ for Le Mas
351 and Villars, and no significant correlation ($p > 0.1$) was observed (Figs. 10C, 10D).

352 The locations of PIMS were determined using 5 days' reconstruction of air
353 mass history during 1997-2016 (Table 4; Fig. 11). Curiously, the most distant areas
354 (NAGR and PAWE) are the principal moisture sources (i.e., roughly $>60\%$), while
355 NA and DA are substantial contributors (i.e., roughly 34%), and the rest of the regions
356 (ME and NESAs) have little impact, at least for the 1997-2016 period (Table 4; Fig.
357 11). On the annual timescale, annual average values for $\delta^{18}\text{O}$ and δD ($\delta^{18}\text{O}_{ap}$ and δD_{ap})
358 were calculated for the same period (Fig. 12A; Appendix Table 3). Annual $\delta^{18}\text{O}_{ap}$
359 value at Le Mas and Villars stations varies from -5.38‰ to -7.24‰ and -5.16‰ to
360 -7.09‰ , respectively (Appendix Table 3). The annual weighted $\delta^{18}\text{O}_p$ means ($\delta^{18}\text{O}_w$)

361 range from -4.63 ‰ to -7.00 ‰ and -4.69 ‰ to -6.79 ‰ for Le Mas and Villars
362 respectively (Appendix Table 3). Whereas the $\delta^{18}\text{O}_p$ has a significant variation at the
363 monthly timescale, it is much lower on the inter-annual timescale (Appendix Table 2,
364 3).

365 We also determine the correlation between PIMS and mean annual precipitation
366 isotope composition ($\delta^{18}\text{O}_{ap}$ and $\delta^{18}\text{O}_w$) for the 1997-2016 period (Fig. 12; Table 4
367 and Appendix Table 2). Results show clear trends in the time-series of stable isotopes
368 in Le Mas and Villars (Figs. 12A, 12B) : $\delta^{18}\text{O}_w$ and $\delta^{18}\text{O}_{ap}$ display a decreasing trend
369 (for both stations Le Mas and Villars) on the 1997-2016 studied period, which
370 coincides to **i**) a decreasing trend of the initial moisture source (PIMS) of closer
371 regions (e.g., PAWE and NA) (Figs. 12C, 12D), and **ii**) to an increasing trend of
372 PIMS of longer pathways (e.g., DA and NAGR) (Figs. 12E, 12F). However, weak or
373 less inter-annual variations for local temperature and precipitation were observed over
374 the past 20 year (Figs. 12G, 12H). In consequence, it appears that most of the
375 inter-annual variability of rainfall isotopic composition ($\delta^{18}\text{O}_p$) is controlled by the
376 variation of the proportion of the different sources characterized by the PIMS trends.

377 The term of d-excess was firstly defined by Dansgaard (1964) as the following
378 equation: $d\text{-excess} = \delta D - 8 \cdot \delta^{18}\text{O}$, illustrating the degree of deviation from the
379 equilibrium of isotopic fractionation caused by the kinetic fractionation in the
380 evaporation of vapor (Dansgaard, 1964). Rainfall d-excess exhibited a weak
381 inter-annual increasing trend in Villars and Le Mas over the past 20 year, and the

382 value range from 17.6 ‰ to -9.0 ‰ with the average value being 10.6 ‰ for Le Mas,
383 and 17.6 ‰ to 1.7 ‰ with the average value being 9.5 ‰ for Villars, respectively
384 (Figs. 13A, 13B), which is close to the value of 10 ‰ for the average of global
385 precipitation. Annual variation of d-excess coincides to an increasing trend of PIMS
386 of longer pathways (e.g., DA and NAGR) and a weak increasing trend in local
387 temperature (Figs. 13A, 13B, 13C, 13D, 13E).

388 **5. Discussions**

389 **5.1 Causes of the variations of precipitation isotope ($\delta^{18}\text{O}_p$, δD_p) in** 390 **SW-France**

391 Whether considering monthly or inter-annual timescale, it appears that $\delta^{18}\text{O}_p$
392 of both Le Mas and Villars stations follow variations of PIMS and local temperature.
393 Several factors may be raised to explain the $\delta^{18}\text{O}_p$ variability: **i)** the length of the
394 water vapor transport route which plays an important role on the Rayleigh
395 fractionation process; **ii)** the initial mean seawater $\delta^{18}\text{O}$ ($\delta^{18}\text{O}_{\text{sw}}$) values which may be
396 different; **iii)** the removal of moisture from an air mass which is
397 temperature-dependent during Rayleigh fractionation, and the progressive
398 condensation of the vapor requires the cooling of the air mass from the vapor of cloud
399 to the falling rain (IAEA working group, 2000).

400 **5.1.1 “amount effect” and “temperature effect” controls**

401 Compared with global meteoric water line (GMWL: $\delta D=8\delta^{18}O+10$) (Craig, 1961;
402 Dansgaard, 1964), we observed that there is a lower slope and a lower intercept in the
403 LMWL of the two monitoring sites (Le Mas and Villars) (Fig. 2C) (Genty et al.,
404 2014). This is a general case for continental stations (IAEA working group, 2000) and
405 may be attributed to evaporation during the precipitation under the clouds and various
406 complex phenomena linked to the history of rainfall (Dansgaard, 1964; Stewart, 1975;
407 Gat, 1996; Peng et al., 2005; Yamanaka et al., 2007; Lachniet, 2009; Pang et al., 2011;
408 Chen et al., 2015; Fig. 2C).

409 A positive correlation is observed between $\delta^{18}O_p$ and local monthly/annual
410 mean temperature (Figs. 3A, 10A, 10B) in Le Mas and Villars. The main reason is
411 that the air mass, after leaving from the moisture source, is dominated by Rayleigh
412 fractionation processes, temperature and “rain-out” dependent (Dansgaard, 1954,
413 1964; Bowen, 2008). Water vapor in the atmosphere is difficult to isothermally
414 condense, and any progress of atmospheric precipitation is caused by a temperature
415 cooling (Dansgaard, 1954, 1964). When the condensed water is formed, then leaving
416 water vapor immediately, the stable isotope ratio is depleted in the condensed water
417 with the decrease of temperature (Dansgaard, 1964; Rozanki et al., 1993; Lachniet,
418 2009).

419 No significant correlation is observed between mean annual precipitation and
420 $\delta^{18}O_p$, suggesting no “amount effect” at the Le Mas and Villars stations (Figs. 3B,

421 10C, 10D; Genty et al., 2014). Additionally, Keklec and Domínguez-Villar (2014)
422 who conducted a monitoring of $\delta^{18}\text{O}_p$ in central Spain, proposed that all climate
423 parameters with a seasonal cycle's characterization would exhibit a certain link with
424 $\delta^{18}\text{O}_p$, however, when monitoring the relationship between single precipitation event
425 with $\delta^{18}\text{O}_p$, these links are not visible (Keklec and Domínguez-Villar, 2014), further
426 indicating that the amount of precipitation is not affecting the $\delta^{18}\text{O}_p$.

427 **5.1.2 Moisture source effect**

428 The transportation distance between moisture source and the monitoring site
429 (latitude effect) has already shown an important control on the $\delta^{18}\text{O}_p$ (Aggarwal et al.,
430 2004; Breitenbach et al., 2010; Chen and Li, 2018). Based on the Rayleigh
431 fractionation process governing these links, the increased moisture transportation
432 distances may result in depleted $\delta^{18}\text{O}_p$ value (Rindsberger et al., 1983; Field, 2010;
433 Krklec and Domínguez-Villar, 2014; Krklec et al., 2018).

434 In winter months, the principal initial moisture sources derive from a longer
435 source (NAGR) in comparison with the summer season characterized by a closer
436 moisture source (PAWE) (Fig. 8). The precipitations that occur during the migration
437 of moisture are enriched in ^{18}O leading to an impoverishment of remaining vapor and
438 then resulting in a lower $\delta^{18}\text{O}_p$ (Araguás-Araguás et al., 2000; Breitenbach et al., 2010;
439 Cai et al., 2016). Therefore, the longer the depression pathway, the lower $\delta^{18}\text{O}_p$ value
440 (Araguás-Araguás et al., 2000; Lee & Fung, 2008; Risi et al., 2008; Lachniet et al.,

441 2009; Kurita, 2013; Cai et al., 2017). The mechanism is similar with “continental
442 effect” where the rainout above the continent is the cause of impoverishment of the
443 $\delta^{18}\text{O}$ with increasing distance from the ocean, but in fact very variable, i.e. from
444 region to region and from season to season (IAEA working group, 2000).

445 Besides, the discrepancy of initial mean sea water $\delta^{18}\text{O}_{\text{sw}}$ values is also an
446 important factor controlling the variation of $\delta^{18}\text{O}_{\text{p}}$ values in SW-France (Rozanski et
447 al., 1993; Clark and Fritz, 1997; Cole et al., 1999; Friedman et al., 2002). Most of the
448 moisture sources in Villars and Le Mas come from two main areas: NAGR in winter
449 and PAWE in summer. Because the mean $\delta^{18}\text{O}_{\text{sw}}$ in the NAGR area (-4.0 ‰ to 0 ‰)
450 (LeGrande and Schmidt, 2006) is lower than the one in the PAWE area (from 0 ‰ to
451 1.5 ‰) (LeGrande and Schmidt, 2006), it may also be a significant contribution to the
452 observed $\delta^{18}\text{O}_{\text{p}}$ variation.

453 An important phenomenon appears at the inter-annual timescale where changes
454 of the $\delta^{18}\text{O}_{\text{w}}$ and $\delta^{18}\text{O}_{\text{ap}}$ follow the inter-annual initial location of moisture source (Fig.
455 12), which is attributed to Rayleigh fractionation process and initial moisture sources
456 (Figs. 11 and 12). Previous works have revealed that the $\delta^{18}\text{O}_{\text{d}}$ (drip-water $\delta^{18}\text{O}$)
457 inherited the signal of atmospheric precipitation on the monthly timescales, and the
458 influence of the “mixing effect” with “old water” in the epikarst zone (Pape et al.,
459 2010; Li et al., 2011; Partin et al., 2013; Zhang & Li, 2019) seriously damp or even
460 suppress the rainfall seasonal characteristics (e.g. heavier in summer and lighter in
461 winter) (Genty et al., 2014), however, other studies indicated that the $\delta^{18}\text{O}_{\text{d}}$ and $\delta^{18}\text{O}_{\text{c}}$

462 can respond to the signal of $\delta^{18}\text{O}_w$ on the interannual timescale (Chen and Li, 2018;
463 Ellis et al., 2020). Our results show that the inter-annual $\delta^{18}\text{O}_p$ and δD_p variations are
464 controlled by the mean annual change of the initial location of moisture source, which
465 provides new insights to explain climatic significance of oxygen isotope of drip water
466 and stalagmites on the interannual timescale in Villars Cave.

467 **5.2 Variations of d-excess on the annual timescale**

468 It is generally believed that d-excess is sensitive to moisture source conditions
469 (Pfahl and Wernli, 2008; Pfahl and Sodemann, 2014), therefore, which is suitable for
470 assessing the origin of water vapor. Moreover, some studies have proposed that high
471 and increasing d-excess values reflect fast evaporation (low RH) and stronger kinetic
472 isotope effects during evaporation (Clark and Fritz, 1997; Dublyansky et al., 2018).

473 The linear variation of d-excess and PIMS of longer pathways (DA and
474 NAGR) exhibits an increasing trend in Le Mas and Villars (Figs. 13A, 13B, 13C,
475 13D), reflecting enhanced evaporations and stronger kinetic isotope effects in the
476 transportation of vapor while moisture from longer pathways was increased over the
477 entire period of observation (Clark and Fritz, 1997; Pfahl and Wernli, 2008;
478 Dublyansky et al., 2018). The increase of air temperature at the monitoring stations
479 over the past 20 years leads to the enhancement of water vapor evaporation, inducing
480 the rising change of precipitation d-excess (Figs. 13A, 13B, 13E). Hence, our results
481 suggest that the d-excess variations in paleo-record (e.g. ice cores) should be adapted

482 to reflect moisture source characterized by atmospheric circulation and local
483 temperature.

484 **5.3 Links between NAO and $\delta^{18}\text{O}_p$ in SW-France**

485 During a positive phase of the NAO, a large pressure gradient between the
486 Azores (High Pressure) and Iceland (Low Pressure) across the North Atlantic creates
487 higher winter temperatures and precipitation over the Atlantic and Northern Europe
488 while it is lower over Mediterranean Sea and North Africa (Hurrell, 1995, 1996; Uvo,
489 2003). The exactly opposite pattern in negative NAO phase is found when the
490 pressure gradient between Azores and Iceland decreases by shifting southwards the
491 northern hemisphere westerly jet-stream (Hurrell, 1995).

492 NAO in different phase plays an important role in the length of water vapor
493 transport in winter and spring (Baldini et al., 2008). When winter and spring NAO
494 index is in positive excursion, warmer westerly winds will carry 18O moisture with
495 shorter transportation distance, resulting in heavier $\delta^{18}\text{O}_p$ values in SW-France
496 (Baldini et al., 2008; Langebroek et al., 2011), therefore NAO index and $\delta^{18}\text{O}_p$ exhibit
497 a positive correlation (Fig. 7A, 7B, 7C, 7D). However, NAO only take a strengthened
498 or weakened effect on the length of water vapor transport in winter (Baldini et al.,
499 2008), which will not change the fact that most of winter moisture source distributed
500 in the region of longer distance (West North Atlantic: North America and Greenland)
501 (Section 4.2; Krklec and Domínguez-Villar, 2014). The isotopic time series at the

502 seasonal timescales show correlations with NAO index, providing a useful NAO
503 proxy ($\delta^{18}\text{O}_p$) to indicate the variation in seasonal paleo-NAO index. However, when
504 it comes to the relationship between NAO and $\delta^{18}\text{O}_p$ in the inter-annual timescale, a
505 particularly weak correlation ($p>0.1$) was found.

506 **5.4 Quantifying the relationship between PIMS/temperature and** 507 **$\delta^{18}\text{O}_p$ in SW-France**

508 The variations of PIMS and local temperature have been identified as important
509 contributors for the observed $\delta^{18}\text{O}_p$ changes in SW-France. Therefore, combining the
510 links between PIMS/temperature and $\delta^{18}\text{O}_p$, several equations were established using
511 multiple linear regression analysis methods as followed:

512 EQ (1) for Le Mas station:

$$513 \delta^{18}\text{O}_p = 0.038 \cdot \text{PAWE} + 0.046 \cdot \text{NA} + 0.054 \cdot \text{ME} + 0.02 \cdot \text{DA} + 0.025 \cdot \text{NAGR} + 0.119 \cdot \text{T} - 10.929,$$

$$514 R = 0.965, p < 0.01$$

515 Where $\delta^{18}\text{O}_p$ indicates precipitation $\delta^{18}\text{O}$ (V-SMOW), and T ($^{\circ}\text{C}$) indicate the local
516 monthly temperature in Le Mas.

517 EQ (2) for Villars station:

$$518 \delta^{18}\text{O}_p = 0.035 \cdot \text{PAWE} + 0.031 \cdot \text{NA} + 0.054 \cdot \text{ME} - 0.001 \cdot \text{DA} + 0.005 \cdot \text{NAGR} + 0.049 \cdot \text{T} - 8.637,$$

$$519 R = 0.942, p < 0.05$$

520 Where $\delta^{18}\text{O}_p$ indicates precipitation $\delta^{18}\text{O}$ (V-SMOW), and T ($^{\circ}\text{C}$) indicate the local
521 monthly temperature in Villars.

522 These two equations allow to evaluate the importance of the factors (PIMS,
523 Temperature) variability on the $\delta^{18}\text{O}_p$ variability. Results show that the following
524 factors influence the $\delta^{18}\text{O}_p$ in the order on importance: Temperature>NAGR>
525 PAWE>NA>DA>ME at the monthly timescale. We use the SPSS software to
526 calculate the variance of contribution rate, and the proportion in the four main
527 principal components are 60.6% (Temperature), 16.6% (NAGR), 15.4% (PAWE), 6.2%
528 (NA), the rest of two-component (DA and ME) is <2%. Therefore, in any case,
529 considering the range of variability of various contributions from different moisture
530 source regions and local temperature, it is obviously found that local temperature is
531 the principal variable controlling the oxygen isotope composition of precipitation in
532 the continental European at a monthly timescale. In addition, adding the different
533 variable step by step and look at the results after each step, we could we found that
534 multiple linear regression is more accurate to describe the relationship between
535 isotopes and water vapor sources and air temperature compared to linear regression
536 methods ([Appendix Table 4](#)).

537 The use of HYSPLIT model for tracking moisture source is providing a good
538 example for how to accurately calculate the relationship between $\delta^{18}\text{O}_p$ and moisture
539 sources. Different from regional/general circulation models of the $\delta^{18}\text{O}_p$ ([Cruz- San](#)
540 [Julián et al., 1992](#); [Celle-Jeanton et al., 2001](#); [Sodemann et al., 2008](#); [Baldini et al.,](#)
541 [2010](#); [Gao et al., 2011](#); [Bershaw et al., 2012](#)), this study not only provides the
542 quantified mathematical equations based among the longest isotopic isotope time

543 series and the variations of PIMS (over 20 years), but also determines the extent of the
544 impact on the monthly timescale.

545 Additionally, the speleothem $\delta^{18}\text{O}$ in the Villars Cave, also recorded a series of
546 abrupt climatic events on the centennial-millennial timescales, such as
547 Dansgaard-Oeschger, Heinrich and 8.2 ka events (Genty et al., 2001, 2003, 2006;
548 Genty, 2008; Wainer et al., 2009, 2010, 2013; Genty et al., 2014). In this study, the
549 long monitoring-based work established a link between local climate parameters and
550 the $\delta^{18}\text{O}_p$, which can be used for interpreting the significance of speleothem $\delta^{18}\text{O}$. No
551 or less correlation was observed between the $\delta^{18}\text{O}_p$ and local precipitation, indicating
552 that speleothem $\delta^{18}\text{O}$ in Villars Cave likely cannot reconstruct local precipitation. In
553 contrast, change in $\delta^{18}\text{O}_p$ can be linked to both the change of moisture source and to
554 the local temperature variation.

555 **6. Conclusions**

556 Based on the observations and models on $\delta^{18}\text{O}_p$ and δD_p , moisture source, and
557 regional/local climate parameters during the 1997-2016 period at the Le Mas and
558 Villars meteorological stations, SW-France, the following conclusions can be drawn:

559 **(1)** Based on HYSPLIT model, we have quantified the percentage of initial moisture
560 source (PIMS) for different months and found shorter transportation distances during
561 summer months and longer ones during winter, which is consistent with the observed
562 seasonal variations of $\delta^{18}\text{O}_p$.

563 (2) The variation of temperature and PIMS are important factors that are the main
564 causes on the seasonal variation of the $\delta^{18}\text{O}_p$. In the order of importance, the
565 following factors influence the $\delta^{18}\text{O}_p$: Temperature>NAGR>PAWE>NA>DA>ME,
566 and the proportion of the four main principal components are 60.6% (Temperature),
567 16.6% (NAGR), 15.4% (PAWE), 6.2% (NA) on the monthly timescale.

568 (3) On the annual timescale, $\delta^{18}\text{O}_p$ maintains a positive relationship with local mean
569 annual temperature, however no evidences for its “amount effect” has been observed.

570 (4) On a longer timescale, an important result shows that an inter-annual decreasing
571 trend was observed for the $\delta^{18}\text{O}_p$ ($\delta^{18}\text{O}_{ap}$ and $\delta^{18}\text{O}_w$), following the variation of annual
572 PIMS. We observed, over the past 20 years, that the percentage of a farther moisture
573 source region (NAGR) was increased, at the opposite, there is a decreasing trend for
574 the closer source (PAWE).

575 (5) The linear variation trend over the past 20 years of d-excess coincides to the
576 variations of PIMS in longer pathways (DA and NAGR) and local temperature on the
577 inter-annual timescale, which is likely due to the global temperature increase and the
578 change of moisture source characterized by atmospheric circulation in SW-France.

579 (6) The variation of moisture distribution regions should be considered when
580 interpreting the climatic significance for speleothem oxygen isotopic records in SW-
581 France.

582 **Acknowledgments**

583 The long monitoring study on Villars Cave was possible thanks to the constant
584 help of the Versaveau family, who have always shown interest in our research.
585 Similarly, Le Mas station rainfall sampling was able to the support of the Genty
586 family during all along these years. We would like to express sincere thanks to Xi Lei
587 for her help in the drawings and Dr. Zhaojun Zhan (school of geography and ocean,
588 Nanjing University, China) for her useful discussions. This research was supported by
589 the China Scholarship Council (CSC) to Jian. Zhang (201906990014). This long
590 monitoring work has been funded, since 1996, by several programs from the CNRS
591 (INSU), and three laboratories (GEOPS, Orsay, Paris-Saclay University; Laboratoire
592 des Sciences du Climat et de l'Environnement, LSCE, CEA/CNRS/UVSQ and
593 Environnements et Paléoenvironnements Océaniques et Continentaux, EPOC,
594 Bordeaux University, France). Le Mas and Villars stations are part of the new French
595 rainfall isotopic network RENOIR SOERE Observatory of the INSU/CNRS.

596 **Competing financial interests**

597 The authors declare no competing financial interests.

598 **References**

599 Abouelmagd, A., Sultan, M., Milewski, A., Kehew, A.E., Sturchio, N.C., Soliman, F.,
600 Krishnamurthy, R.V., Curtim, E., 2012. Towards a better understanding of palaeoclimatic
601 regimes that recharged the fossil aquifers in North Africa: Inferences from stable isotope and
602 remote sensing data. *Palaeogeogr., Palaeoclim., Palaeoecol.* 329-330, 137–149.

603 Aggarwal, P.K., Frohlich, K., Kulkarni, K.M., Gourcy, L.L., 2004. Stable isotope evidence for
604 moisture sources in the Asian summer monsoon under present and past climate regimes.
605 *Geophys. Res. Lett.* 31(8).

606 Allen, S. T., Kirchner, J. W., & Goldsmith, G. R. (2018). Predicting spatial patterns in
607 precipitation isotope ($\delta^2\text{H}$ and $\delta^{18}\text{O}$) seasonality using sinusoidal isoscapes. *Geophysical*
608 *Research Letters*, 45, 4859– 4868. <https://doi.org/10.1029/2018GL077458>.

609 Alley, R.B., Cuffey, K.M., 2001. Oxygen- and hydrogen-isotopic ratios of water in precipitation:
610 beyond paleothermometry. *Rev. Mineral. Geochem.* 43, 527–553.

611 Araguás-Araguás, L. J., and M. F. Diaz Teijeiro. 2005. Isotope composition of precipitation and
612 water vapour in the Iberian Peninsula: first results of the Spanish network of isotopes in
613 precipitation. *At. Energy. Agency. Tech. Report 1453*: 173-190.

614 Araguás-Araguás, L., Froehlich, K., Rozanski, K., 2000. Deuterium and oxygen-18 isotope
615 composition of precipitation and atmospheric moisture. *Hydro. process*, 14(8), 1341–1355.

616 Baldini, L.M., McDermott, F., Foley, A.M., Baldini, J.U.L., 2008. Spatial variability in the
617 European winter precipitation $\delta^{18}\text{O}$ -NAO relationship: Implications for reconstructing
618 NAO-mode climate variability in the Holocene. *Geophys. Res. Lett.* 35(4), L04709.

619 Breitenbach, S.F.M. et al. Breitenbach, S. F., Adkins, J. F., Meyer, H., Marwan, N., Kumar, K. K.,
620 Haug, G. H., 2010. Strong influence of water vapor source dynamics on stable isotopes in
621 precipitation observed in Southern Meghalaya, NE India. *Earth Planet. Sci. Lett.* 292(1-2):0–
622 220.

623 Bowen, G.J., 2008. Spatial analysis of the intra-annual variation of precipitation isotope ratios and
624 its climatological corollaries. *J. Geophys. Res. Atmos.* 113.

625 Cassou, C., Terray, L., Hurrell, J. W., Deser, C., 2004. North Atlantic winter climate regimes:
626 Spatial asymmetry, stationarity with time, and oceanic forcing. *J. Clim.* 17(5), 1055–1068.

627 Cai, Z., Tian. L., Bowen, G. J., 2017. ENSO variability reflected in precipitation oxygen isotopes

628 across the Asian Summer Monsoon region. *Earth Planet. Sci. Lett.* 475:25–33.

629 Celle-Jeanton H., Travi Y. and Blavoux B., 2001. Isotopic typology of the precipitation in the
630 western Mediterranean region at three different timescales. *Geophys. Res. Lett.* 28(7), 1215–
631 1218.

632 Chen, B., A. F. Stein, N. Castell, J. D. de la Rosa, A. M. Sanchez de la Campa, Y.
633 Gonzalez-Castanedo., R. R. Draxler., 2012., Modeling and surface observations of arsenic
634 dispersion from a large Cu-smelter in southwestern Europe. *Atmos. Environ.*, 49, 114–122.

635 Chen, C-J., Li, T-Y. 2018. Geochemical characteristics of cave drip water respond to ENSO based
636 on a 6-year monitoring work in Yangkou cave, Southwest China, *J. Hydrol*, 561:896–907.

637 Chen, F. L., Zhang, M. J., Wang, S. J., Ma, Q., Zhu, X. F., Dong, L., 2015. Relationship between
638 sub-cloud secondary evaporation and stable isotopes in precipitation of Lanzhou and
639 surrounding area, *Quatern. Int.*, 380-381, 68–74.

640 Clark, I., Fritz, P., 1997. *Environmental Isotopes in Hydrology*. Lewis Publishers, New York.

641 Cole, J.E., Rind, D., Webb, R.S., Jouzel, J., Healy, R., 1999. Climatic controls on interannual
642 variability of precipitation $\delta^{18}\text{O}$: Simulated influence of temperature, precipitation amount, and
643 vapor source region. *J. Geophys. Res.*, 104, 14223–14235.

644 Craig, H., 1961. Isotopic variations in meteoric waters. *Science*. 133(3465): 1702–1703.

645 Craig, H., Gordon, L.I., 1965. Deuterium and oxygen 18 variations in the ocean and the marine
646 atmosphere, *The stable isotopes in oceanographic studies and paleotemperatures*, Lab. Geol.
647 Nucl., Pisa, Italy, 9–130.

648 Crawford, J., Hughes, C. E., Lykoudis, S. 2014. Alternative least squares methods for determining
649 the meteoric water line, demonstrated using GNIP data. *J. Hydrol*, 519, 2331-2340.

650 Cruz-San Julian, J. L. Araguas, K. Rozanski, J. Benavente, J. Cardenal, M. C. Hidalgo, S.
651 Garcia-Lopez, J. C. Martinez-Garrido, F. Moral & M. Olias., 1992. Sources of precipitation
652 over South-Eastern Spain and groundwater recharge. An isotopic study, *Tellus B: Chemical*

653 and Physical Meteorology, 44:3, 226–236.

654 Dansgaard, W., 1954. The O¹⁸-abundance in fresh water. *Geochim.Cosmochim. Acta.* 6, 241–260.

655 Dansgaard, W., 1964. Stable isotopes in precipitation. *Tellus* 16, 436–468.

656 Draxler, R. R., Hess, G. D., 1998. An overview of the HYSPLIT_4 modelling system for
657 trajectories, dispersion and deposition. *Aust. Meteorol. Mag.* 47(4), 295–308.

658 Draxler, R. R., and G. D. Rolph., 2010. HYSPLIT (HYbrid Single-Particle Lagrangian Integrated
659 Trajectory) model access via NOAA ARL READY website (<http://ready.arl.noaa.gov/HYSPLIT.php>). NOAA Air Resources Laboratory. Silver Spring, MD, 25.

660

661 Duffourg, F., Ducrocq, V., 2011. Origin of the moisture feeding the Heavy Precipitating Systems
662 over Southeastern France. *Nat. Hazard. Earth. Sys.* 11(4), 1163.

663 Dumitru, O.A., Forray, F.L., Fornós, J.J., Ersek, V., Onac, B.P., 2017. Water isotopic variability in
664 Mallorca: a path to understanding past changes in hydroclimate. *Hydrol. Process.* 31, 1, 104–
665 116.

666 Dublyansky, Y. V., Klimchouk, A. B., Tokarev, S. V., Amelichev, G. N., Langhamer, L., Spötl, C.
667 2018. Stable isotopic composition of atmospheric precipitation on the Crimean Peninsula and
668 its controlling factors. *J. Hydrol*, 565, 61-73.

669 Ellis, S. A, Cobb, K. M., Moerman, J. W., Partin, J. W., Bennett, A. L., Malang, J., Gerstner, H.,
670 Tuen, A.A., Extended cave drip water time series captures the 2015–2016 El Niño in Northern
671 Borneo. *Geophys. Res. Lett.*, 2020, 47(5).

672 Field, R.D., 2010. Observed and modeled controls on precipitation δ¹⁸O over Europe: From local
673 temperature to the Northern Annular Mode, *J. Geophys. Res.* 115, D12101.

674 Fischer, M. J., D. Matthey., 2012. Climate variability and precipitation isotope relationships in the
675 Mediterranean region. *J. Geophys. Res. Atmos.* 117.D20.

676 Fricke H. C., O’Neil J. R., 1999. The correlation between ¹⁸O/¹⁶O ratios of meteoric water and

677 surface temperature: its use in investigating terrestrial climate change over geologic time.
678 Earth Planet. Sci. Lett. 170, 181–196.

679 Friedman, I., Harris, J.M., Smith, G.I., Johnson, C.A., 2002. Stable isotope composition of waters
680 in the Great Basin, United States, 1, Air-mass trajectories, J. Geophys. Res. 107(D19), 4400.

681 Gat, J.R., 1996. Oxygen and hydrogen isotopes in the hydrologic cycle. Annu. Rev. Earth. Planet.
682 Sci.24, 225–262.

683 Gat. J. R., 2010. Isotope Hydrology: A Study of the Water Cycle. Imperial College Press, London.

684 Genty. D., Baker. A., Massault. M., Proctor. C., Gilmour. M., PonsBranchu. E., Hamelin B., 2001.
685 Dead carbon in stalagmites: carbonate bedrock paleodissolution vs. ageing of soil organic
686 matter. Implication for ¹³C variation in speleothems. Geochim.Cosmochim. Acta 65, 3443–
687 3457.

688 Genty, D., Blamart, D., Ouahdi, R., Gilmour, M., Baker, A., Jouzel, J., & Van-Exter, S. 2003.
689 Precise dating of Dansgaard–Oeschger climate oscillations in western Europe from stalagmite
690 data. Nature, 421(6925), 833.

691 Genty. D., Blamart. D., Ghaleb. B., Plagnes. V., Causse. C., Bakalowicz. M., Zouari. K., Chkir.N.,
692 Hellstrom. J., Wainer. K., Bourges. F., 2006. Timing and dynamics of the last deglaciation
693 from European and North African delta C-13 stalagmite profiles – comparison with Chinese
694 and South Hemisphere stalagmites. Quatern. Sci. Rev. 25, 2118–2142.

695 Genty. D., 2008. Palaeoclimate research in Villars Cave (Dordogne, SW-France). Int. J. Speleol.
696 37, 173–191.

697 Genty, D., Labuhn, I., Hoffmann, G., Danis, P.A., Mestre, O., Bourges, F., Wainer, K., Massault,
698 M., Van Exter, S., Régnier, E., Orengo, Ph., Falourd, S., Minster, B., 2014. Rainfall and cave
699 water isotopic relationships in two South-France sites. Geochim. Cosmochim. Acta. 131 (5),
700 323–343.

701 Giuntoli, I., Renard, B., Vidal, J. P., Bard, A., 2013, Low flows in France and their relationship to

702 large-scale climate indices. *J. Hydrol*, 482: 105-118.

703 Hoffmann, G., Werner, M., Heimann, M., 1998. The Water isotope module of the ECHAM
704 atmospheric general circulation model - A study on time scales from days to several years. *J.*
705 *Geophys. Res.* 103, 16,871–16,896.

706 Hu, C.Y. et al., 2008. Quantification of Holocene Asian monsoon rainfall from spatially separated
707 cave records. *Earth Planet. Sci. Lett.* 266(3):221–232.

708 Hughes, C. E., Crawford, J. 2012. A new precipitation weighted method for determining the
709 meteoric water line for hydrological applications demonstrated using Australian and global
710 GNIP data. *J. Hydrol.* 464, 344-351.

711 Hurrell, J.W., 1995. Decadal trends in the north Atlantic oscillation: regional temperatures and
712 precipitation, *Science*, 269, 676-679.

713 Hurrell, J. W., 1996, Influence of variations in extratropical wintertime teleconnections on
714 Northern Hemisphere temperature, *Geophys. Res. Lett.*, 23, 665- 668.

715 IAEA Publish chapter 4. 2000. Environmental isotopes in the hydrological cycle. 39.

716 Krklec, K., Domínguez-Villar, D., Lojen, S., 2018. The impact of moisture sources on the oxygen
717 isotope composition of precipitation at a continental site in central Europe, *J. Hydrol.*, 561,
718 810–821.

719 Krklec. Kristina., David. Domínguez-Villar., 2014. Quantification of the impact of moisture
720 source regions on the oxygen isotope composition of precipitation over Eagle Cave, central
721 Spain. *Geochim. Cosmochim. Acta.* 134: 39–54.

722 Kurita, N. 2013. Water isotopic variability in response to meso-scale convective system over the
723 tropical ocean. *J. Geophys. Res. Atmos.*, 118, 10 376–10 390.

724 Lachniet. M. S., 2009. Climatic and environmental controls on speleothem oxygen-isotope values.
725 *Quatern. Sci. Rev.* 28, 412–432.

726 Ladouche. Bernard., Aquilina. Luc., Dörfliger. Nathalie., 2009. Chemical and isotopic

727 investigation of rainwater in Southern France (1996–2002): Potential use as input signal for
728 karst functioning investigation. *J. Hydro.* 367.1-2: 150–164.

729 Langebroek, P.M., Werner, M., Lohmann, G., 2011. Climate information imprinted in
730 oxygen-isotopic composition of precipitation in Europe. *Earth Planet. Sci. Lett.* 311(1–2):144–
731 154.

732 Lee, J.-E., Fung, I., 2008. “Amount effect” of water isotopes and quantitative analysis of
733 post-condensation processes. *Hydrol. Processes*, 22, 1–8, doi:10.1002/hyp.6637.

734 LeGrande, A.N., Schmidt, G.A., 2006. Global gridded data set of the oxygen isotopic composition
735 in seawater. *Geophys. Res. Lett.* 33.

736 Li, T.-Y., Shen, C.-C., Li, H.-C., Li, J.-Y., Chiang, H.-W., Song, S.-R., Yuan, D.-X., Lin, C.D.J.,
737 Gao, P., Zhou, L.-P., Wang, J.-L., Ye, M.-Y., Tang, L.-L., Xie, S.-Y., 2011. Oxygen and
738 carbon isotopic systematics of aragonite speleothems and water in Furong Cave, Chongqing,
739 China. *Geochim. Cosmochim. Acta.* 75(15), 4140-4156.

740 McDermott, F., Atkinson, T. C., Fairchild, I. J., Baldini, L. M., Matthey, D. P., 2011. A first
741 evaluation of the spatial gradients in delta (18)O recorded by European Holocene speleothems.
742 *Global Planet. Change* 79, 275–287.

743 McCarthy, G. D., Haigh, I. D., Hirschi, J. J. M., Grist, J. P., Smeed, D. A. 2015. Ocean impact on
744 decadal Atlantic climate variability revealed by sea-level observations. *Nature*, 521(7553),
745 508-510.

746 Numaguti, A., 1999. Origin and recycling processes of precipitating water over the Eurasian
747 continent: Experiments using an atmospheric general circulation model. *J. Geophys. Res.*
748 *Atmos.* 104, 1957–1972.

749 O'Reilly, C. H., Huber, M., Woollings, T., Zanna, L. 2016. The signature of low-frequency
750 oceanic forcing in the Atlantic Multidecadal Oscillation. *Geophys. Res. Lett.* 43(6), 2810-2818.

751 Pang, Z. H., Kong, Y. L., Froehlich, K., Huang, T. M., Yuan, L. J., Li, Z. Q., Wang, F. T., 2011.

752 Processes affecting isotopes in precipitation of an arid region, *Tellus. B.*, 63, 352–359.

753 Pape, J. R., Banner, J. L., Mack, L. E., Musgrove, M., Guilfoyle, A., 2010. Controls on oxygen
754 isotope variability in precipitation and cave drip waters, central Texas, USA. *J.*
755 *Hydrol*, 385(1-4), 203–215.

756 Partin, J. W. Cobb, K. M., Adkins, J. F., Tuen, A. A., Clark, B. 2013. Trace metal and carbon
757 isotopic variations in cave drip water and stalagmite geochemistry from northern Borneo.
758 *Geochem. Geophys. Geosyst.* 14(9):3567–3585.

759 Peng, H., Mayer, B., Norman, A. L., Krouse, H. R., 2005. Modelling of hydrogen and oxygen
760 isotope compositions for local precipitation. *Tellus B.* 57(4), 273–282.

761 Petit, J.R., Jouzel, J., Raynaud, D., Barkov, N.I., Barnola, J.-M., Basile, I., Bender, M., Chappellaz,
762 J., Davis, M., Delaygue, G., Delmotte, M., Kotlyakov, V.M., Legrand, M., Lipenkov, V.Y.,
763 Lorius, C., Pepin, L., Ritz, C., Saltzman, E., Stievenard, M., 1999. Climate and atmospheric
764 history of the past 420,000 years from the Vostok ice core, Antarctica. *Nature* 399, 429–436.

765 Pfahl, S. and Sodemann, H., 2014. What controls deuterium excess in global precipitation?
766 *Climate of the Past*, 10(2), pp.771-781.

767 Pfahl, S., Wernli, H., 2008. Air parcel trajectory analysis of stable isotopes in water vapor in the
768 eastern Mediterranean. *J. Geophys. Res.* 113: D20104.

769 Risi, C., Bony, S., Vimeaux, F., 2008. Influence of convective processes on the isotopic
770 composition ($\delta^{18}\text{O}$ and δD) of precipitation and water vapour in the tropics: 2 Physical
771 interpretation of the amount effect. *J. Geophys. Res.* 113, D19306.

772 Rolph, G. D., Coauthors, 2009. Description and verification of the NOAA Smoke Forecasting
773 System: The 2007 fire season. *Wea. Forecasting*, 24, 361–378.

774 Rozanski, K., Araguás-Araguás, L., Gonfiantini, R., 1993. Isotopic patterns in modern global
775 precipitation. In: Swart, P.K., Lohmann, K.L., McKenzie, J., Savin, S. (Eds.), *Climate Change*
776 *in Continental Isotopic Records*. American Geophysical Union, Washington, DC, pp. 1–37.

777 Sánchez - Murillo, R., Esquivel - Hernández, G., Corrales - Salazar, J. L., Castro - Chacón, L.,
778 Durán - Quesada, A. M., Guerrero - Hernández, M., Delgado, V., Barberena, J.,
779 Montenegro-Rayó. K., Calderón. Heyddy., Chevez, C., Peña-Paz. T., García-Santos, Saúl.,
780 Ortiz-Roque, Pedro., Alvarado-Callejas, Y., Benegas, L., Hernández-Antonio, A., Matamoros-
781 Ortega, M., Ortega, L. Terzer-Wassmuth, S. Chevez, C. (2020). Tracer hydrology of the
782 data - scarce and heterogeneous Central American Isthmus. *Hydrological Processes*.
783 2020;1–16

784 Schmidt, G.A., LeGrande, A.N., Hoffmann, G., 2007. Water isotope expressions of intrinsic and
785 forced variability in a coupled ocean-atmosphere model, *J. Geophys. Res.* 112, D10103.

786 Sharp, Z., 2007. *Principles of Stable Isotope Geochemistry*. Pearson Prentice Hall, Upper Saddle
787 River, NJ.

788 Sodemann, H., Schwierz, C., Wernli, H., 2008. Interannual variability of Greenland winter
789 precipitation sources: Lagrangian moisture diagnostic and North Atlantic Oscillation
790 influence. *J. Geophys. Res.* 113, D03107.

791 Stein, A.F., Draxler, R.R., Rolph, G.D., Stunder, B.J.B., Cohen, M.D., Ngan, F., 2015. NOAA's
792 HYSPLIT atmospheric transport and dispersion modeling system, *Bull. Amer. Meteor. Soc.*,
793 96, 2059–2077.

794 Stewart, M. K. 1975. Stable isotope fractionation due to evaporation and isotopic exchange of
795 falling waterdrops: Applications to atmospheric processes and evaporation of lakes, *J.*
796 *Geophys. Res.*, 80, 1133-1146.

797 Sturm, K., Hoffmann, G., Langmann, B., Stichler, W., 2005. Simulation of ^{18}O in precipitation by
798 the regional circulation model REMOiso. *Hydrol. Process.* 19, 3425–3444.

799 Tang, Y., Pang, H., Zhang, W., Li, Y., Wu, S., Hou, S., 2015. Effects of changes in moisture
800 source and the upstream rainout on stable isotopes in summer precipitation – a case study in
801 Nanjing, East China, *Hydrol. Earth. Syst. Sc.*, 12, 3919–3944.

802 Uemura, R., Masson-Delmotte, V., Jouzel, J., Landais, A., Motoyama, H., Stenni, B., 2012.

803 Ranges of moisture-source temperature estimated from Antarctic ice cores stable isotope
804 records over glacial-interglacial cycles, *Clim. Past*, 8, 1109–1125.

805 Vo, C. B., 2003, Analysis and regionalization of Northern European winter precipitation based on
806 its relationship with the North Atlantic Oscillation, *Int. J. Climatol.*, 23, 1185-1194.

807 Wang, Y.J., Cheng, H., Edwards, R.L., An, Z.S., Wu, J.Y., Shen, C.C., Dorale, J.A., 2001.A
808 high-resolution absolute-dated Late Pleistocene monsoon record from Hulu Cave, China.
809 *Science*. 294, 2345–2348.

810 Wainer K., Genty D., Blamart D., Hofmann D., Couchoud I., 2009, A new stage 3 millennial
811 climatic variability record from a SW France speleothem, *Palaeogeogr., Palaeoclim.,*
812 *Palaeoecol.*, 271: 130-139.

813 Wainer K., Genty D., Blamart D., Daëron M., Bar-Matthews M., Vonhof H., Dublyansky
814 Y., Pons-Branchu E., Thomas L., van Calsteren P., Quinif Y. and Caillon N., 2011,
815 Speleothem record of the last 180 ka in Villars cave (SW France):Investigation of a large
816 d18O shift between MIS6 and MIS5, *Quatern. Sci. Rev.*, 30:130-146.

817 Wainer K., Genty D., Blamart D., Bar-Matthews M., Quinif Y., Plagnes V., 2013, Millennial
818 climatic instability during penultimate glacial period recorded in a south-western France
819 speleothem., *Palaeogeogr., Palaeoclim., Palaeoecol.*, 376:122-131.

820 Yamanaka, T., Tsujimura, M., Oyunbaatar, D., Davaa, G., 2007. Isotopic variation of precipitation
821 over eastern Mongolia and its implication for the atmospheric water cycle, *J. Hydrol.*, 333, 21–
822 34.

823 Zhang, J., Li. Ting-Yong., 2019. Seasonal and inter-annual variation of hydro-chemical
824 characteristics and stable isotopic compositions of drip waters in Furong Cave, Southwest
825 China based on 12 years' monitoring. *J. Hydrol.* 572:40-50.

826 Zhang, P.Z., Cheng, H., Edwards, R.L., Chen, F.H., Wang, Y.J., Yang, X.L., Liu, J., Tan, M.,
827 Wang, X.F., Liu, J.H., An, C.L., Dai, Z.B., Zhou, J., Zhang, D.Z., Jia, J.H., Jin, L.Y., Johnson,
828 K.R., 2008. A test of climate, sun and culture relationship from an 1810-year Chinese cave

829

record. Science 322, 940–942.

830 **Caption**

831 **Figure 1** Location of the two monitoring stations. **(A)** Location of the study area,
832 including Villars (a, blue point) and Le Mas (b, red point) in SW-France. The range of
833 initial $\delta^{18}\text{O}_{\text{sw}}$ value is from 0 to 1.5 ‰ in PAWE (see Appendix Table 1 for areas
834 names), 0.5 to 2.0 ‰ in DA, 0 to 0.5 ‰ in NA, -4.0 to 0 ‰ in NAGR, 1.5 to 2.5 ‰ in
835 ME, and 0 to 1.0 ‰ in NENA (referred and modified from Lachniet, 2009; Krklec and
836 Domínguez-Villar, 2014). **(B)** Geomorphologic map and site distribution for the
837 surrounding of the Villars and Le Mas stations. The arrow indicates the direction of
838 the initial moisture source.

839 **Figure 2** Time series of monthly rainfall $\delta^{18}\text{O}_p$ at Villars **(A)** and Le Mas **(B)**
840 monitoring stations. **(C)** Local meteoric water line (LMWL) for Le Mas (red), and
841 Villars (blue) based on the linear regression. The Global Meteoric Water Line
842 (GMWL) in green (Craig, 1961) is plotted for comparison.

843 **Figure 3 (A)** Correlation between rainfall $\delta^{18}\text{O}_p$ and local monthly temperature for the
844 1997-2016 period. **(B)** Correlation between rainfall $\delta^{18}\text{O}_p$ and local monthly
845 precipitation for the 1997-2016 period.

846 **Figure 4** Seasonal correlation maps between $\delta^{18}\text{O}_p$ from Le Mas (top panel) and
847 Villars (bottom panel) and temperatures over Europe during the period of 1997-2016
848 (Some disconnected data is not considered). **(A, E)** DJF, **(B, F)** MMA, **(C, G)** JJA, **(D,**

849 **H)** SON. Black crosses indicate grid points where the correlation is not significant at
850 the 90% confidence level. However, the discontinuities of $\delta^{18}\text{O}_p$ data was excluded in
851 some years ([Appendix data](#)). The figure was produced using the programming
852 language R. The degrees of freedom corrections were calculated by timeseries
853 autocorrelations ([McCarthy et al., 2015](#)).

854 **Figure 5** Seasonal correlation maps between $\delta^{18}\text{O}_p$ from Le Mas (top panel) and
855 Villars (bottom panel) and precipitation over Europe during the period of 1997-2016
856 (Some disconnected data is not considered). (**A, E**) DJF, (**B, F**) MMA, (**C, G**) JJA, (**D,**
857 **H)** SON. Black crosses indicate grid points where the correlation is not significant at
858 the 90% confidence level. However, the discontinuities of $\delta^{18}\text{O}_p$ data was excluded in
859 some years ([Appendix data](#)). The figure was produced using the programming
860 language R. The degrees of freedom corrections were calculated by timeseries
861 autocorrelations ([McCarthy et al., 2015](#)).

862 **Figure 6** Seasonal correlation maps between $\delta^{18}\text{O}_p$ from Le Mas (top panel) and
863 Villars (bottom panel) stations and SST in North Atlantic during the 1997-2016
864 period (Some disconnected data is not considered). (**A, E**) DJF, (**B, F**) MMA, (**C, G**)
865 JJA, (**D, H**) SON. Black crosses indicate grid points where the correlation is not
866 significant at the 90% confidence level. However, the discontinuities of $\delta^{18}\text{O}_p$ data
867 was excluded in some years ([Appendix data](#)). The figure was produced using R
868 programming language. The degrees of freedom corrections were calculated by
869 timeseries autocorrelations ([McCarthy et al., 2015](#)).

870 **Figure 7 (A)** Correlation between $\delta^{18}\text{O}_p$ and NAO index at Le Mas during the winter
871 period of 1997-2016. **(B)** Correlation between $\delta^{18}\text{O}_p$ and NAO index at Villars during
872 the winter period of 1997-2016. **(C)** Correlation between $\delta^{18}\text{O}_p$ and NAO index at Le
873 Mas during the spring period of 1997-2016. **(D)** Correlation between $\delta^{18}\text{O}_p$ and NAO
874 index at Villars during the winter period of 1997-2016.

875 **Figure 8** Back trajectories for contrasted seasons, winter (December **(A)**, January **(B)**,
876 February **(C)**) and summer (June **(D)**, July **(E)**, August **(F)**). The star indicates the
877 location of Villars, and the detailed data of PIMS is listed in Table 2. The air mass
878 history was calculated at 1500 m a.g.l over the past 120 hours, and every 6 hours
879 outputted a trajectory, then we integrated all of the calculated data into ten trajectories.
880 The back trajectories are presented for monthly variations for the period of
881 1997-2016.

882 **Figure 9** Back trajectories for March **(A)**, April **(B)**, May **(C)**, September **(D)**,
883 October **(E)** and November **(F)**. The star indicates the location of Villars, and the
884 detailed data of moisture source is listed in Table 1. The air mass history was
885 calculated at 1500 m a.g.l over the past 120 hours, and every 6 hours outputted a
886 trajectory, then we integrated all of the calculated data into ten trajectories.

887 **Figure 10 (A)** Correlation between annual mean precipitation $\delta^{18}\text{O}$ ($\delta^{18}\text{O}_{ap}$) and local
888 annual mean temperature at Le Mas. **(B)** Correlation between $\delta^{18}\text{O}_{ap}$ and local annual
889 mean temperature at Villars. **(C)** Correlation between $\delta^{18}\text{O}_{ap}$ and local annual mean

890 precipitation at Le Mas. **(D)** Correlation between $\delta^{18}\text{O}_{\text{ap}}$ and local annual mean
891 precipitation at Villars.

892 **Figure 11** Back trajectories for initial moisture sources for the 1997-2016 period. The
893 star indicates the location of Villars, and the detailed data of moisture source is listed
894 in Table 2. The air mass history was calculated at 1500 m a.g.l over the past 120 hours,
895 and every 6 hours outputted a trajectory, then we have integrated all of the calculated
896 data into ten trajectories.

897 **Figure 12** Comparison of $\delta^{18}\text{O}_{\text{ap}}$ and the percentage of initial moisture source (PIMS)
898 and local annual mean temperature and precipitation at Le Mas and Villars on the
899 inter-annual timescale. **(A)** the inter-annual variation of average weighted
900 precipitation $\delta^{18}\text{O}$ ($\delta^{18}\text{O}_{\text{w}}$), **(B)** the inter-annual average variation of precipitation $\delta^{18}\text{O}$
901 ($\delta^{18}\text{O}_{\text{ap}}$), **(C)** the inter-annual variation of PAWE, **(D)** the inter-annual variation of NA,
902 **(E)** the inter-annual variation of DA, **(F)** the inter-annual variation of NAGR. **(G)** the
903 inter-annual variation of local annual mean temperature in Villars. **(H)** the
904 inter-annual variation of local annual mean precipitation in Villars. The fitting dashed
905 lines indicated the trend for the changes on the inter-annual timescale.

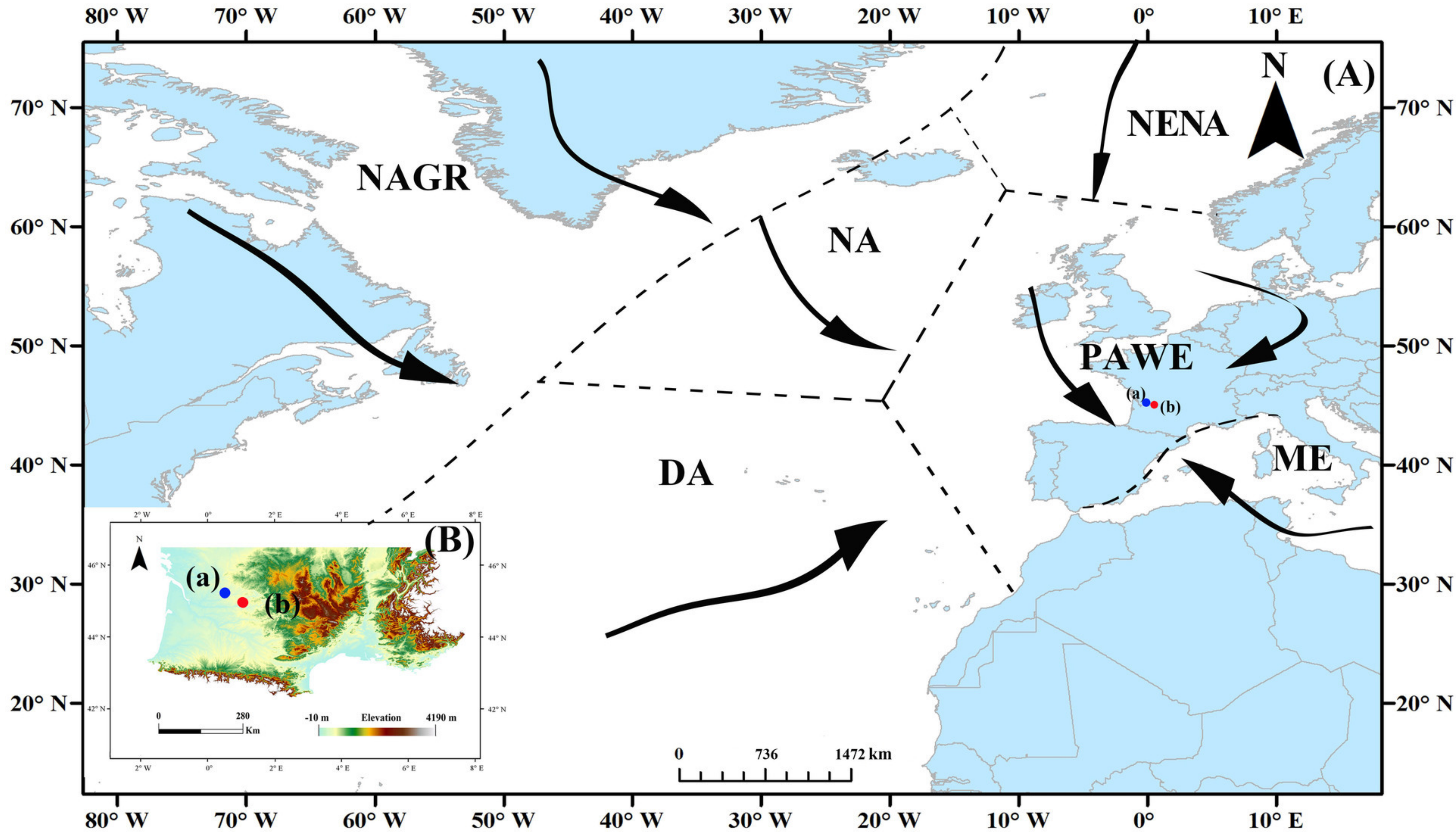
906 **Figure 13** Comparison of the d-excess with the percentage of initial moisture source
907 (PIMS) and the local annual mean temperature at Le Mas and Villars on the
908 inter-annual timescale. **(A)** inter-annual variation of the d-excess at Villars, **(B)**
909 inter-annual variation of the d-excess at Le Mas, **(C)** the inter-annual variation of DA,
910 **(D)** inter-annual variation of NAGR. **(E)** inter-annual variation of local annual mean

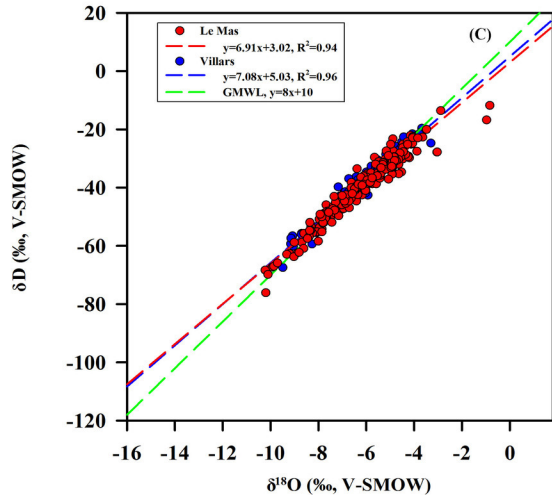
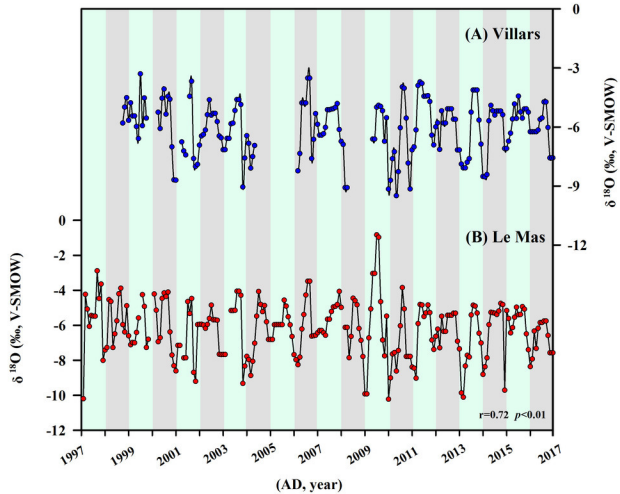
911 temperature in Villars. The fitting dashed lines indicates the trend for the changes on

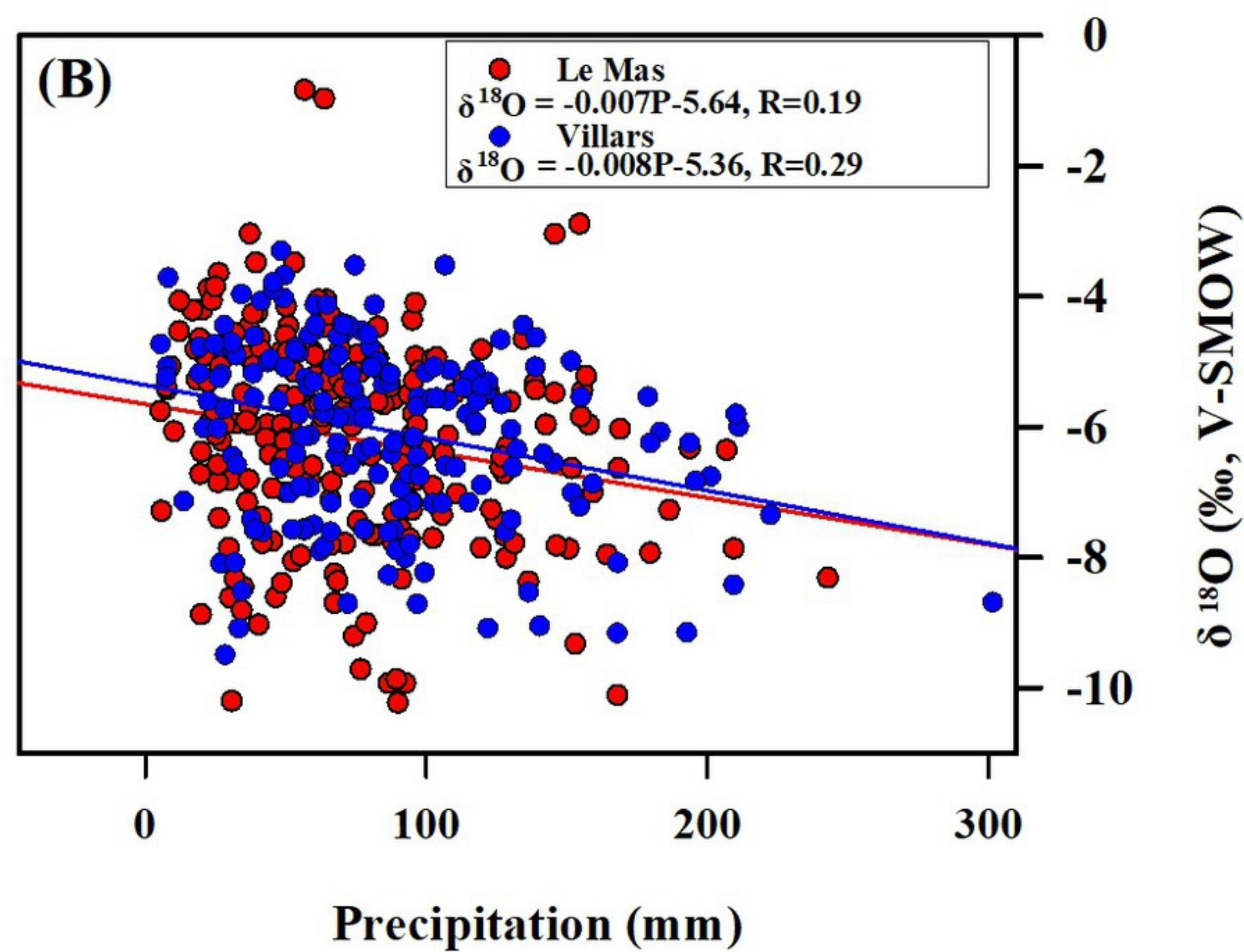
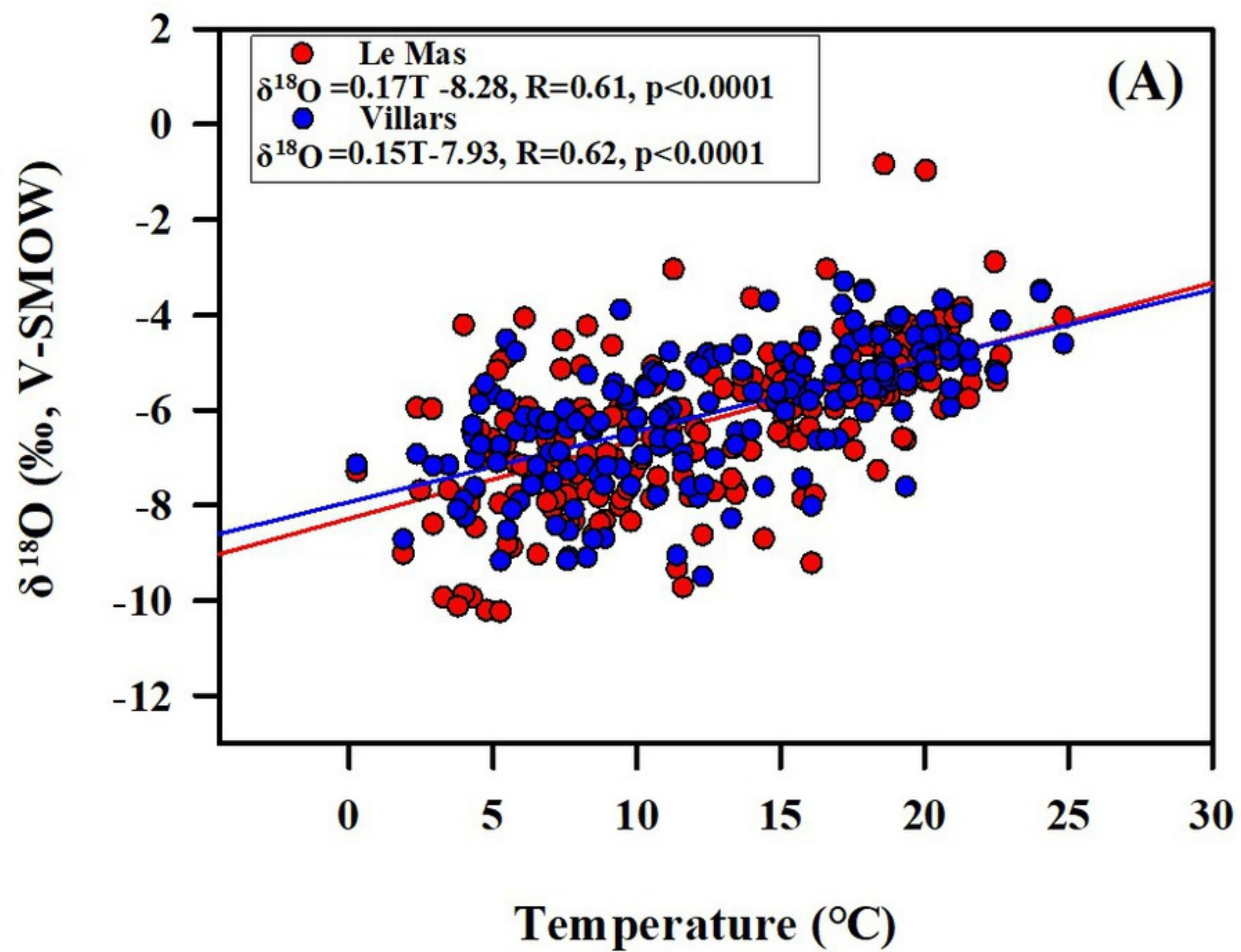
912 the inter-annual timescale.

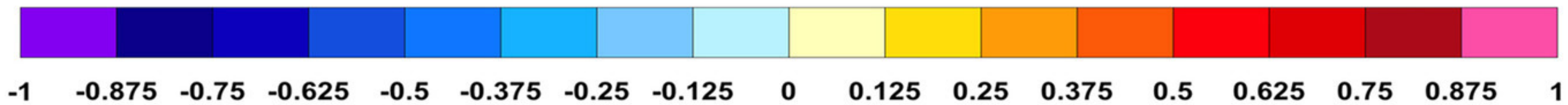
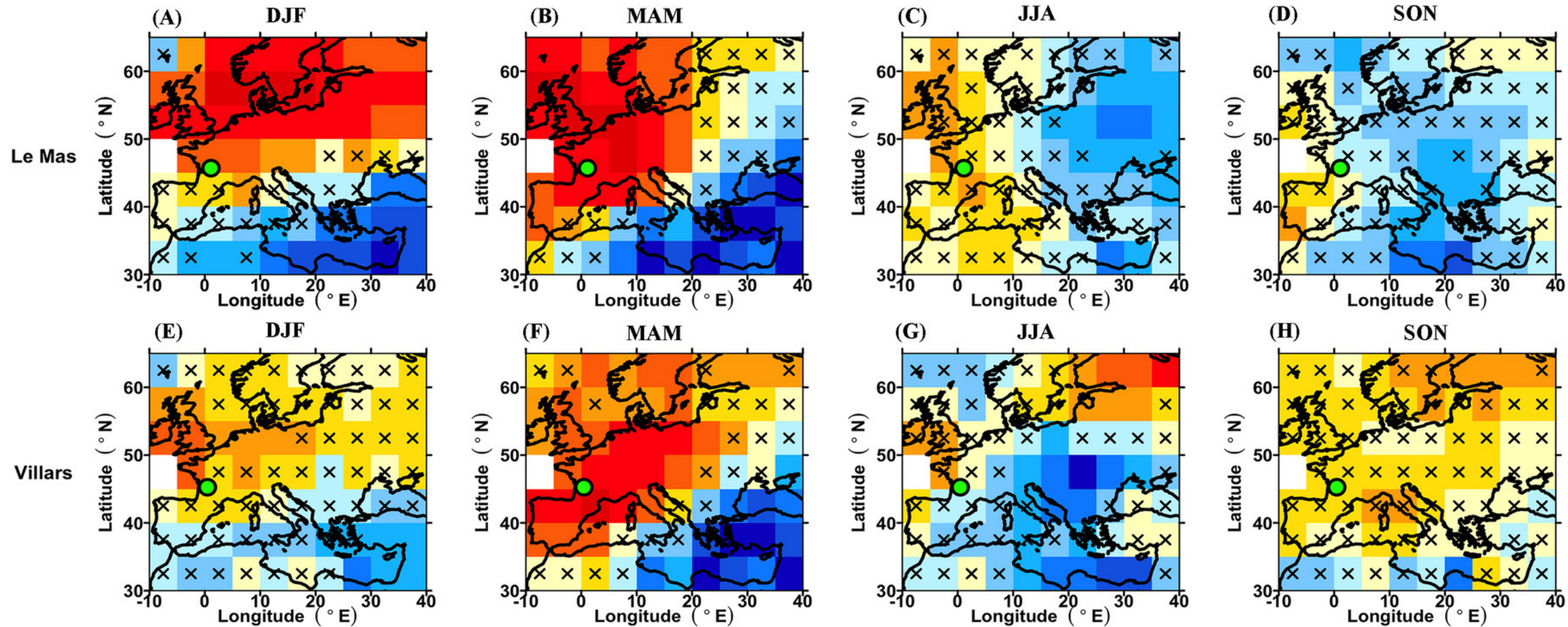
913

914

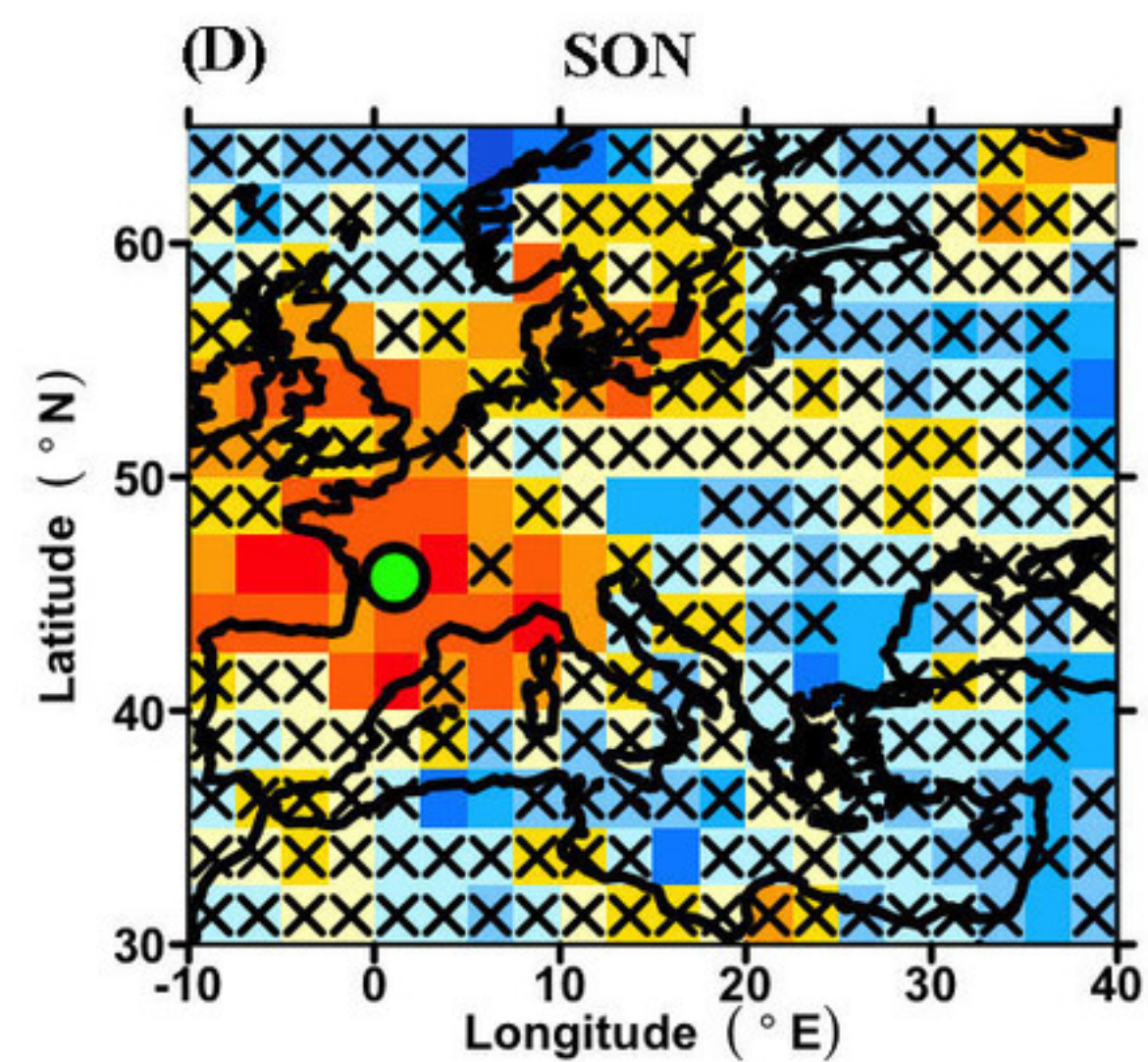
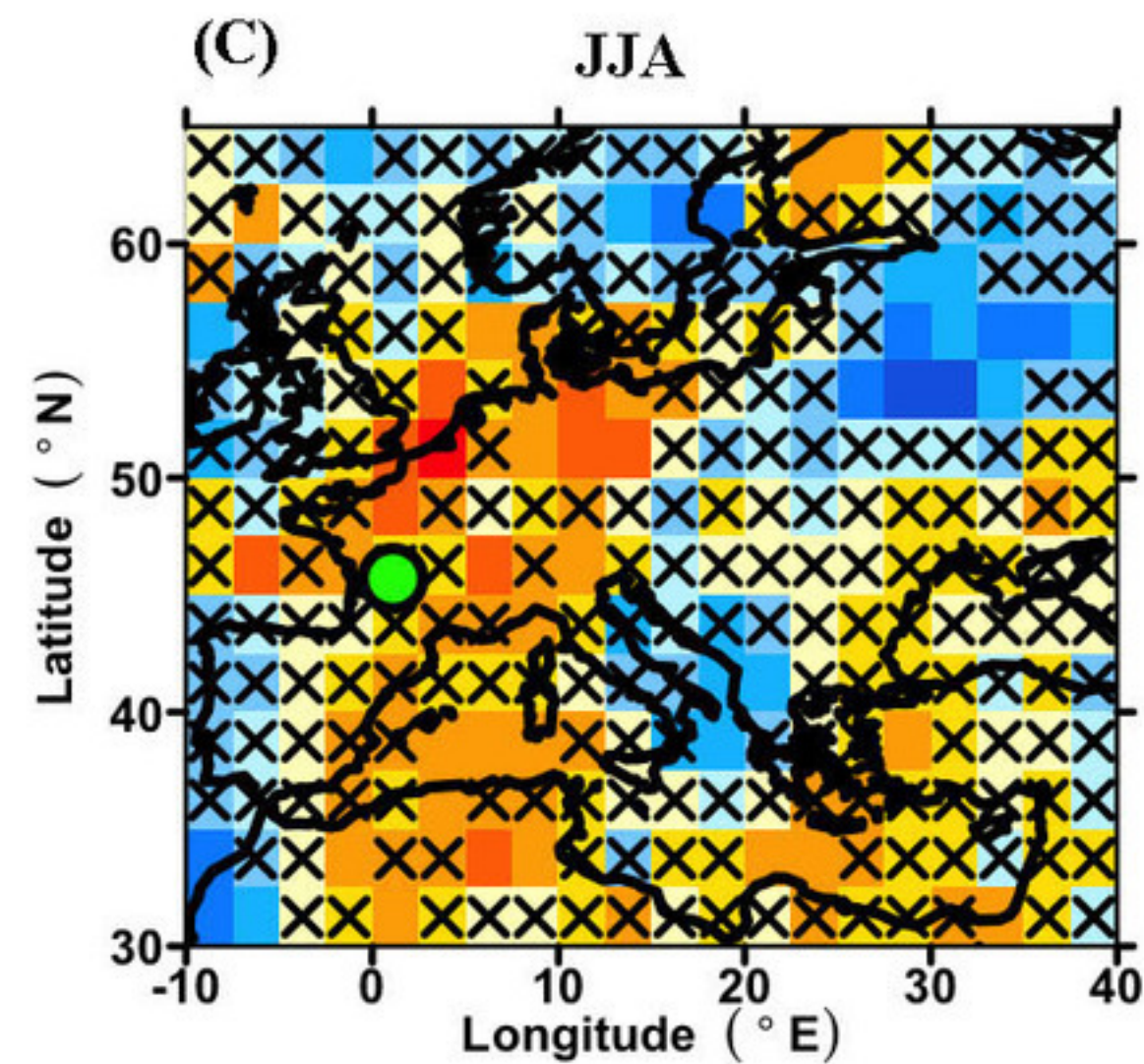
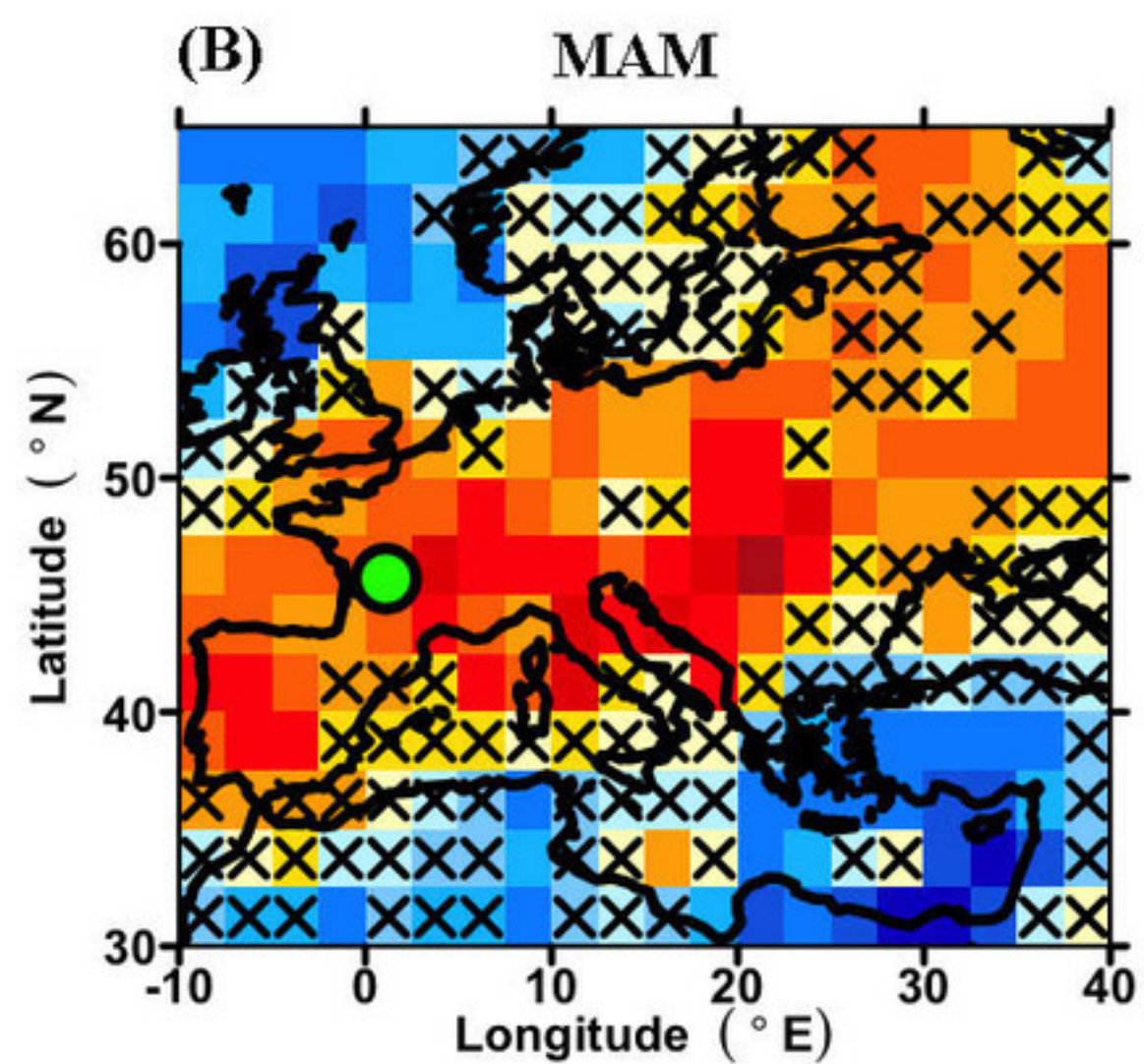
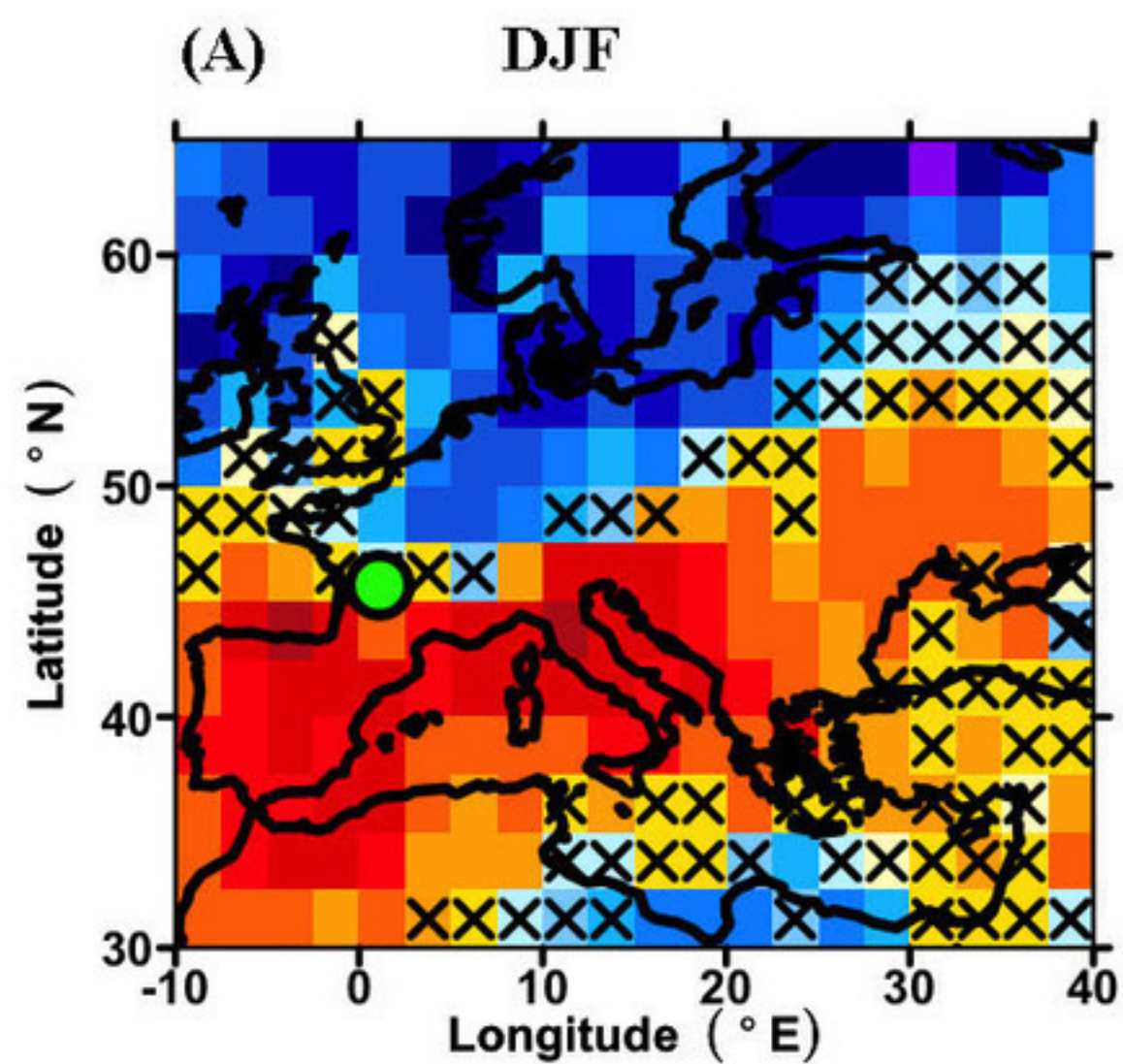




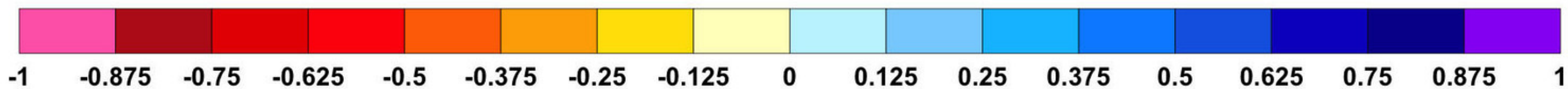
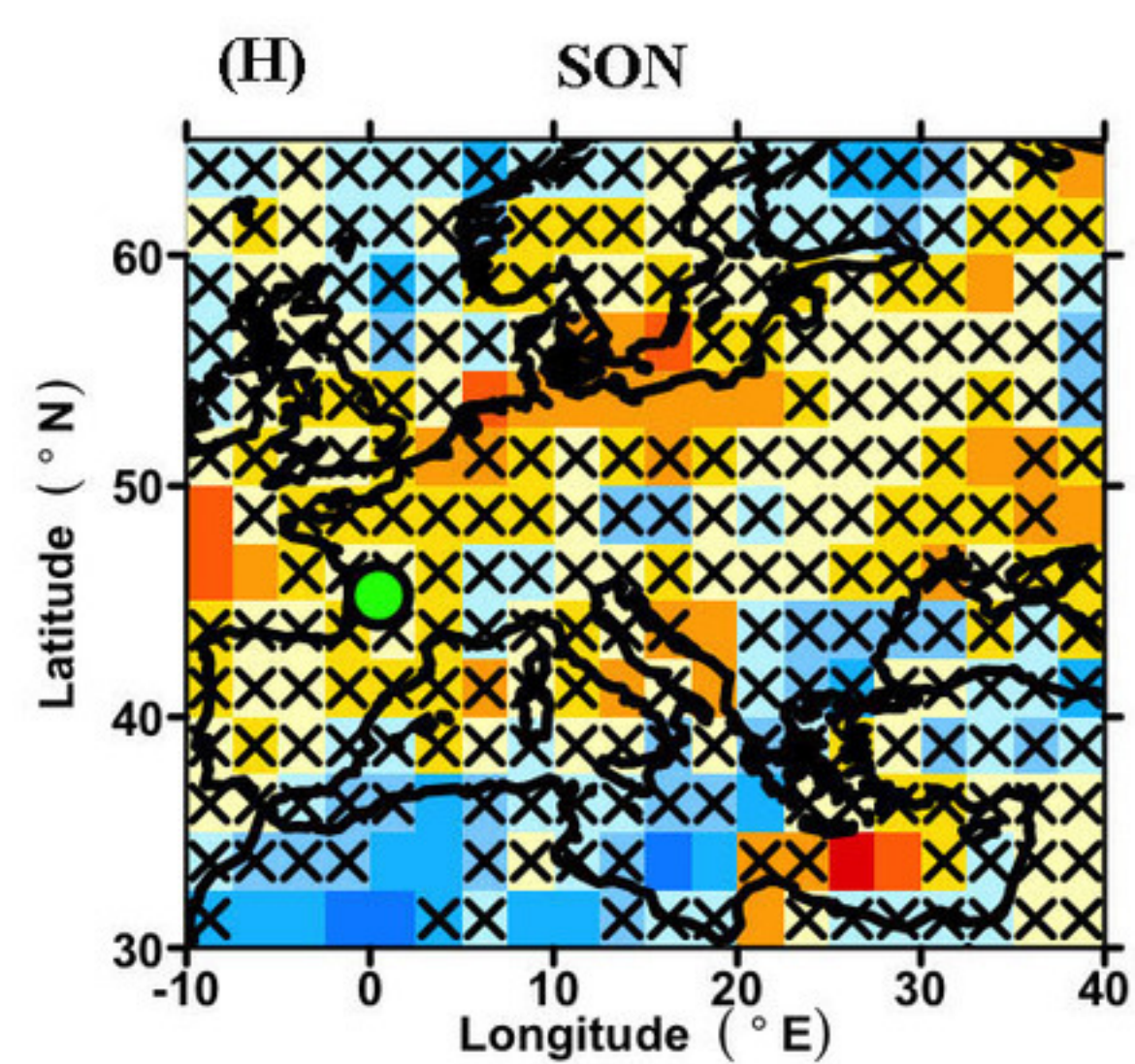
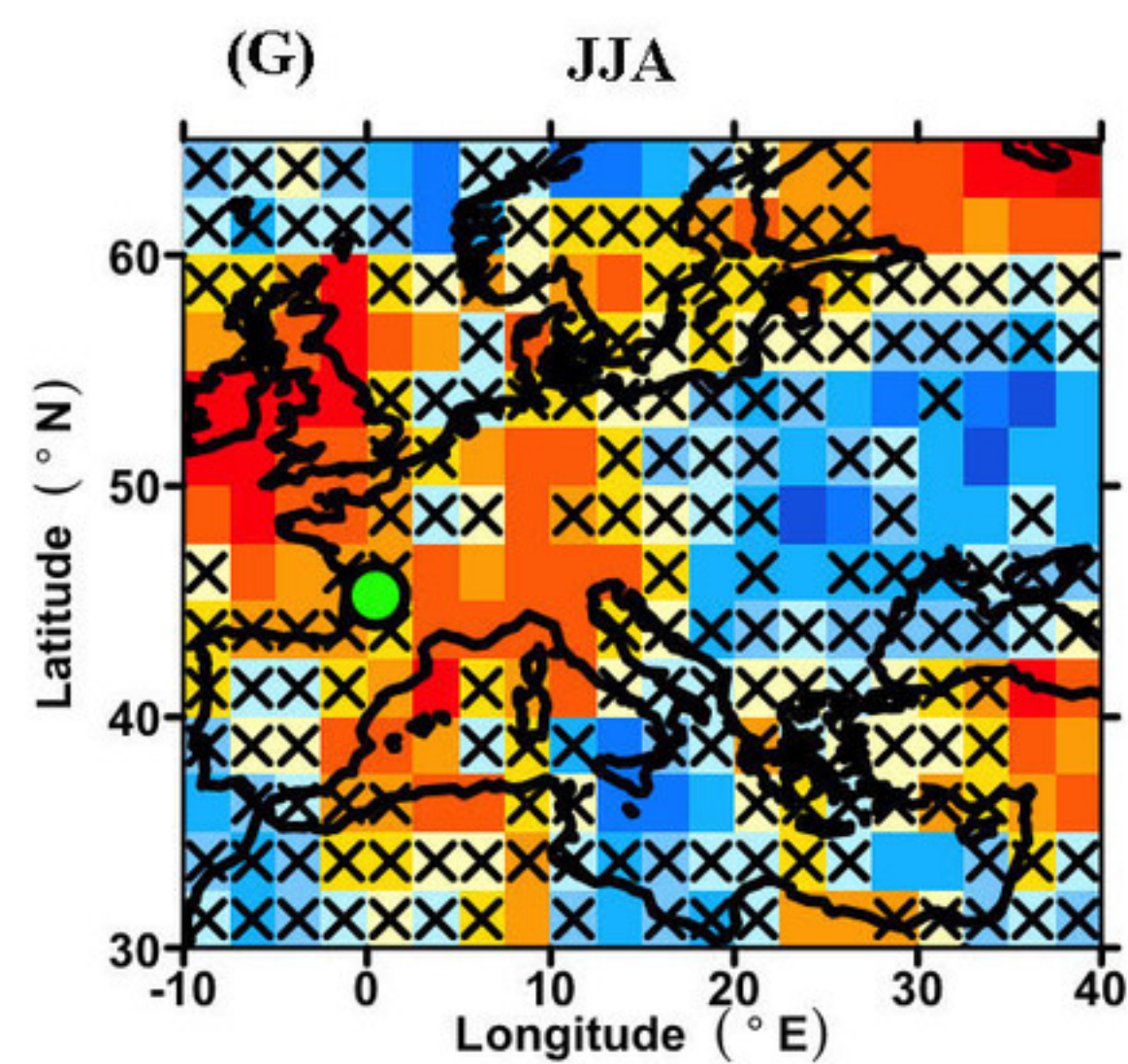
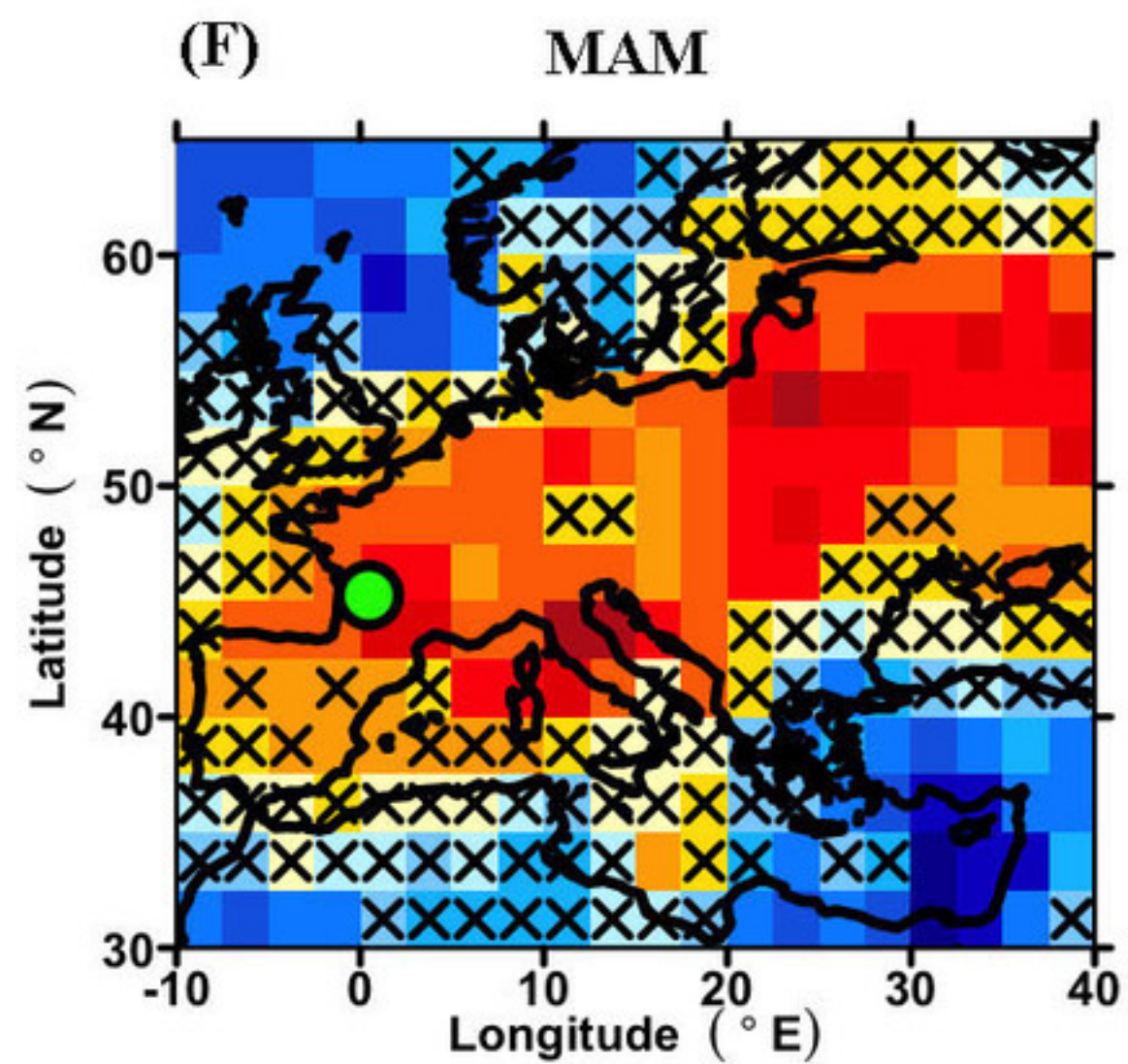
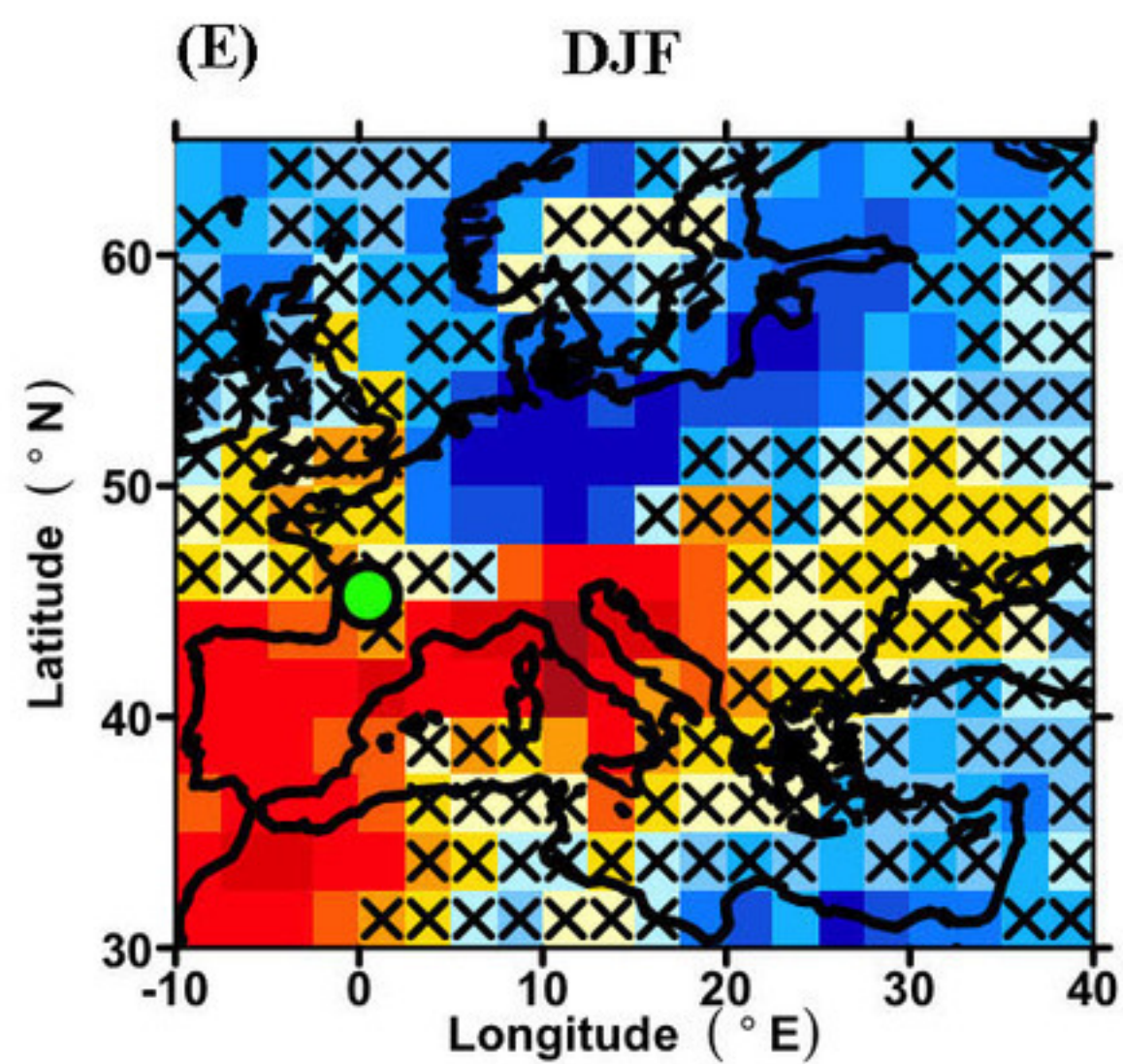


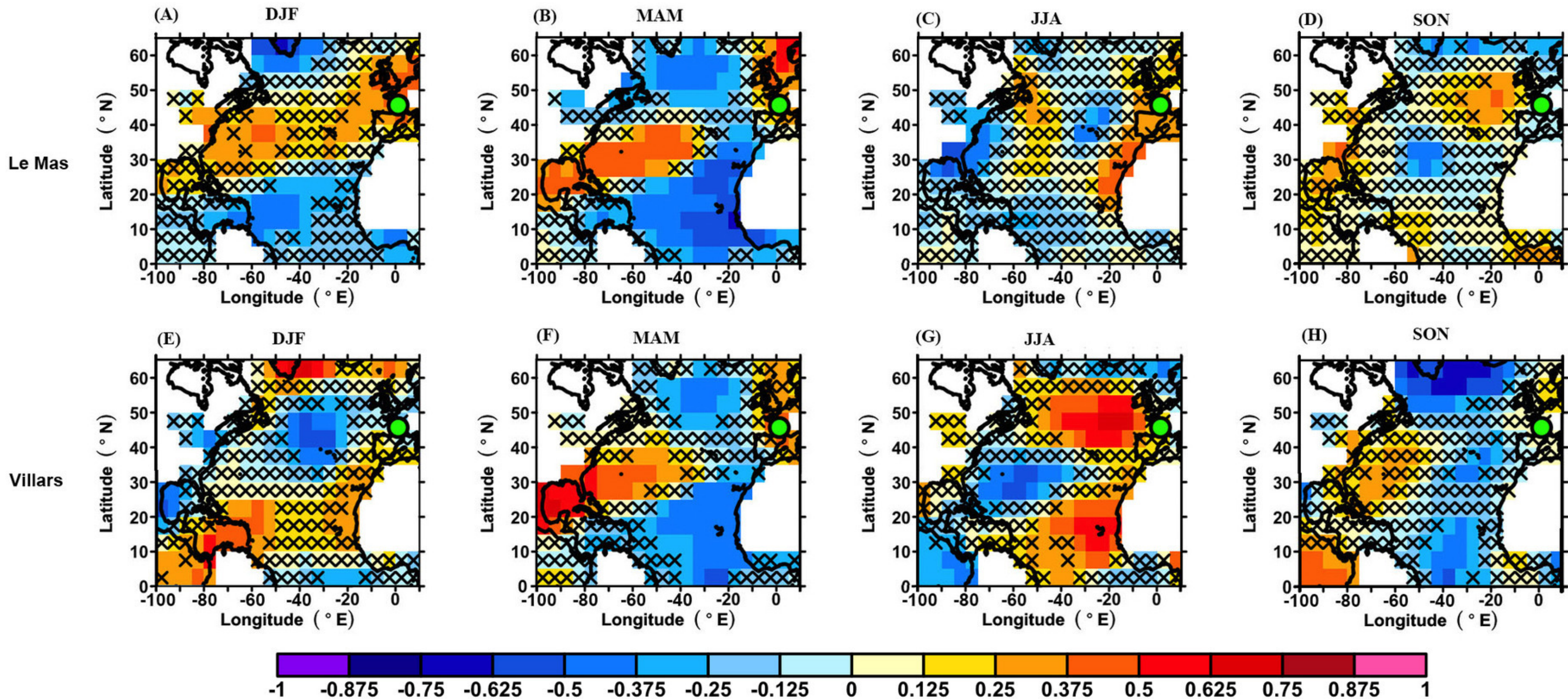


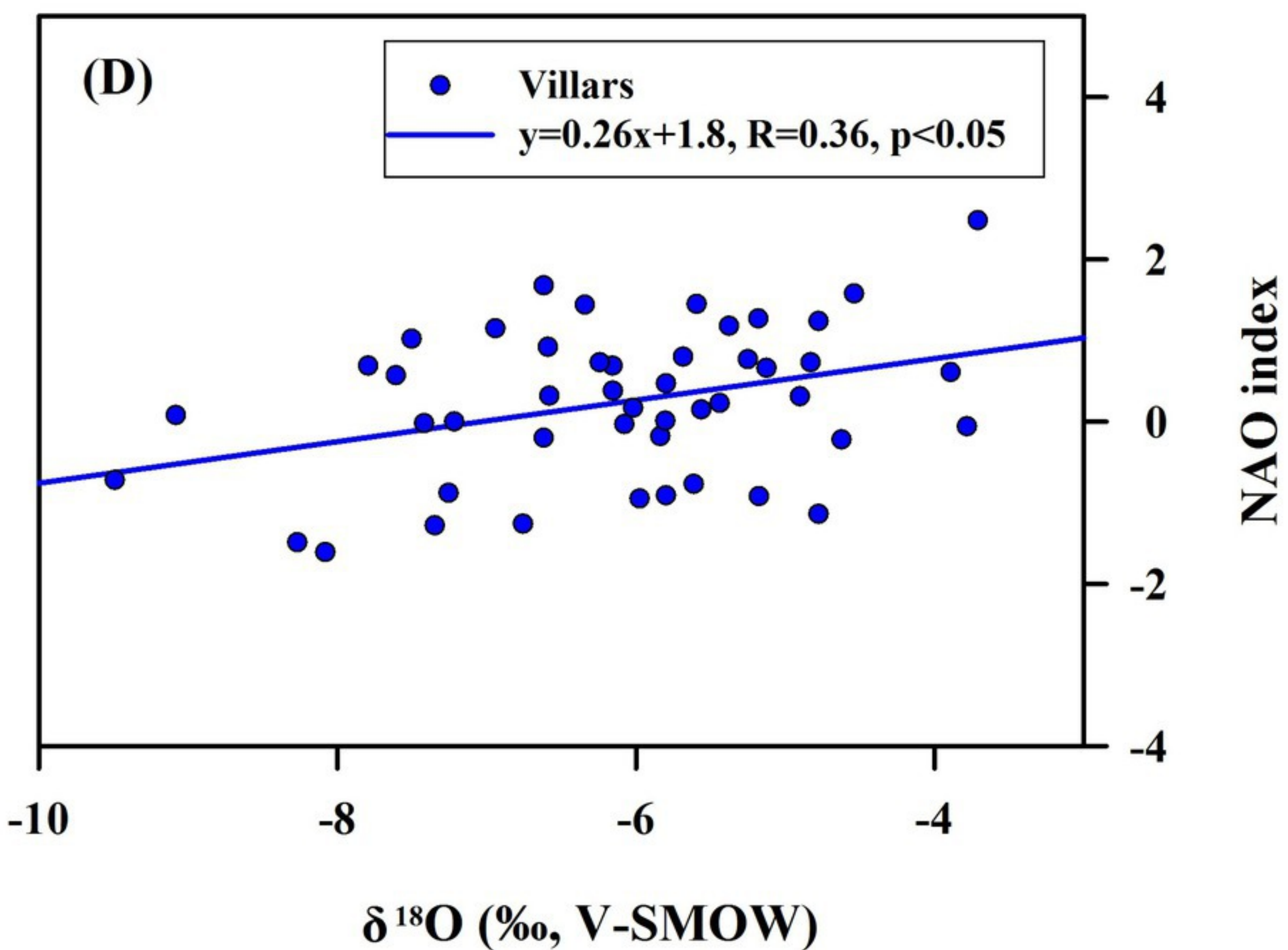
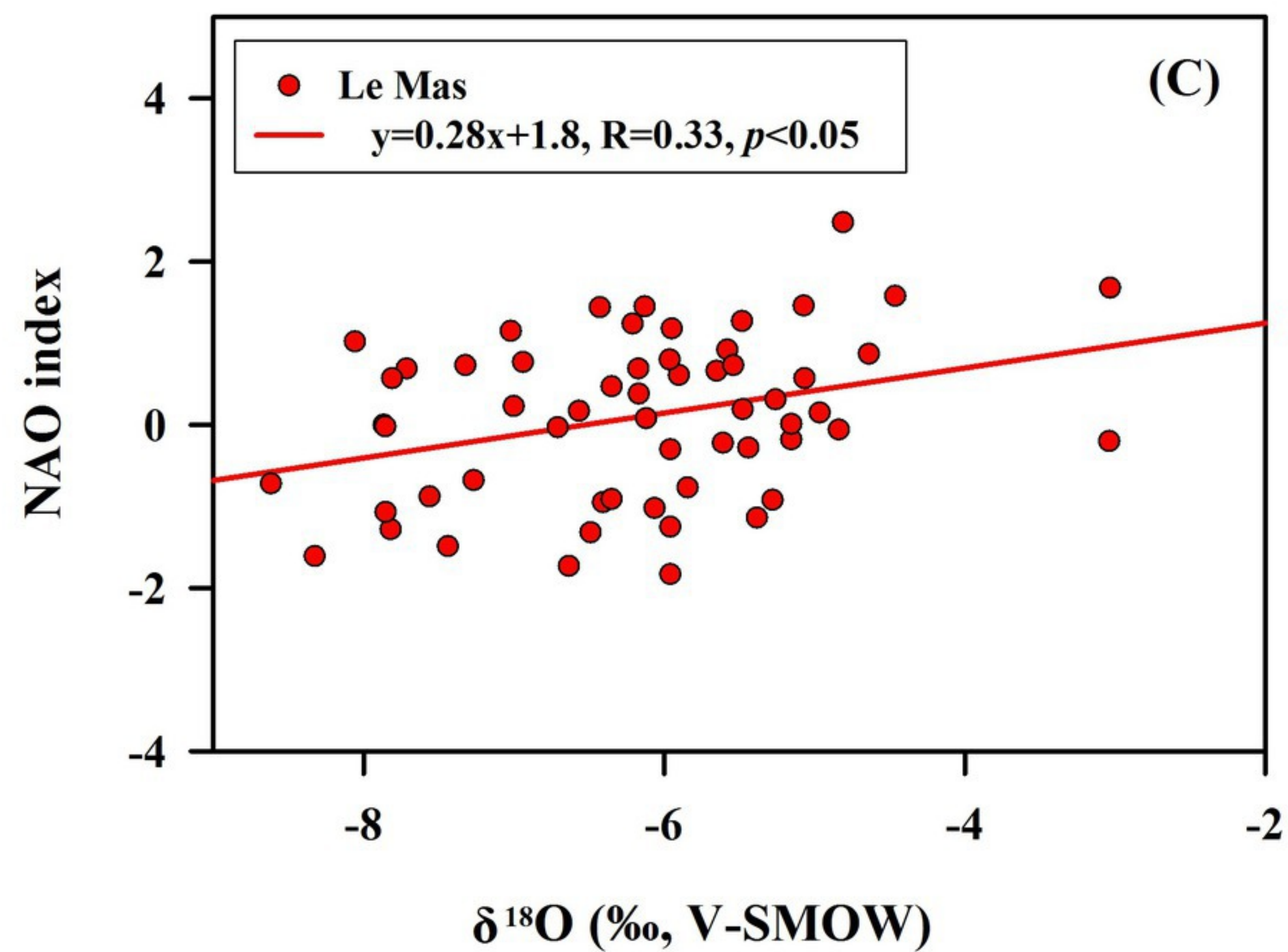
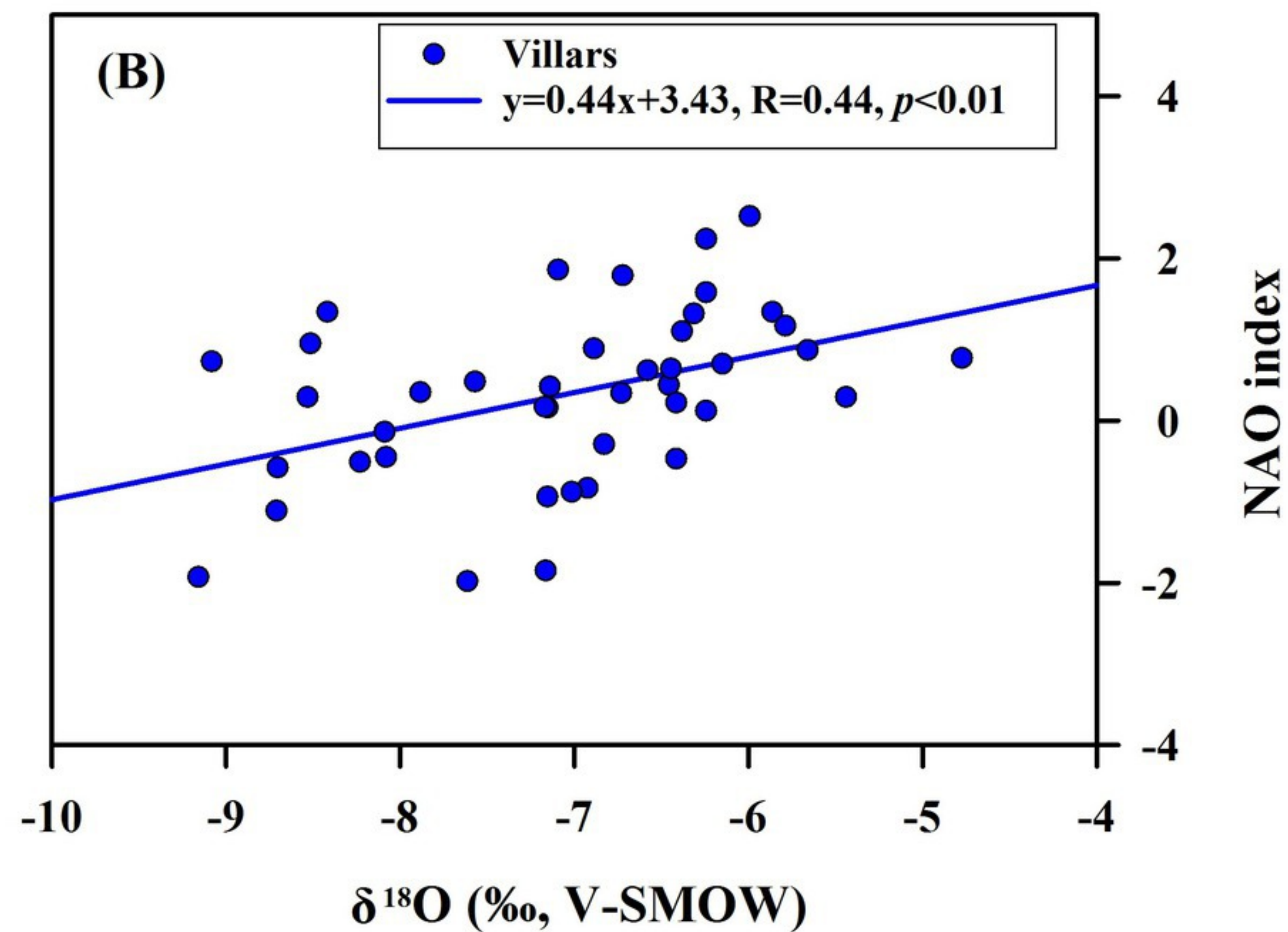
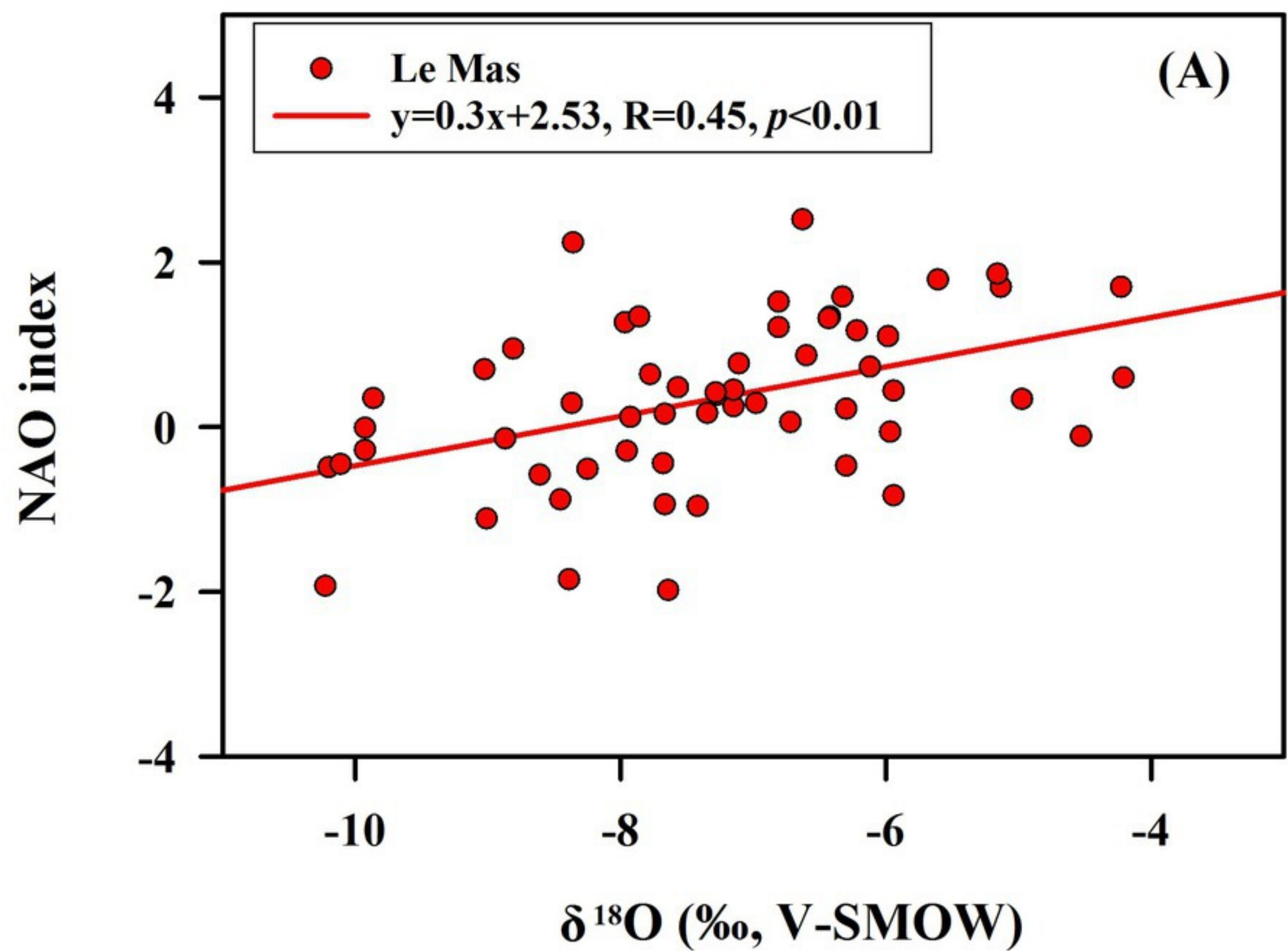
Le Mas

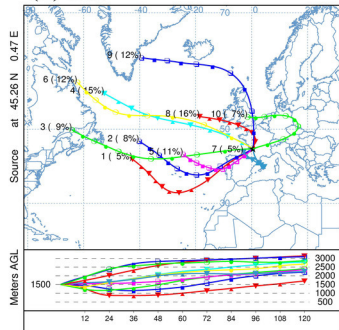
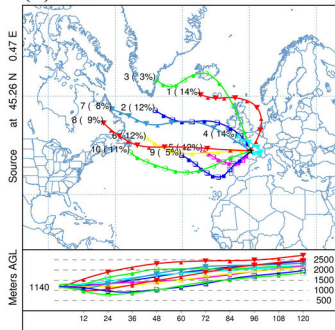
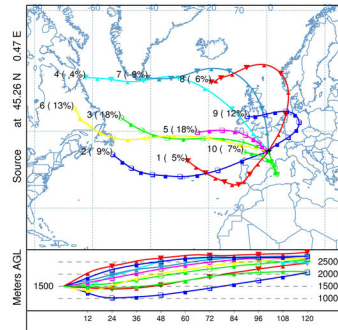
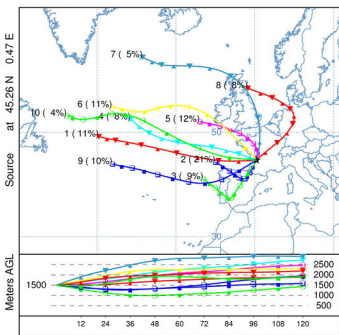
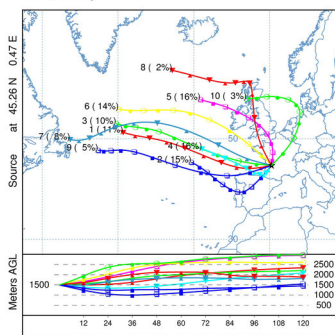
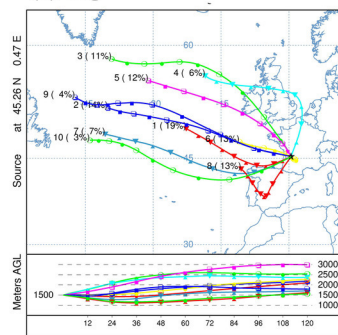


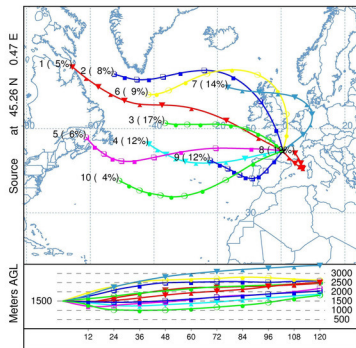
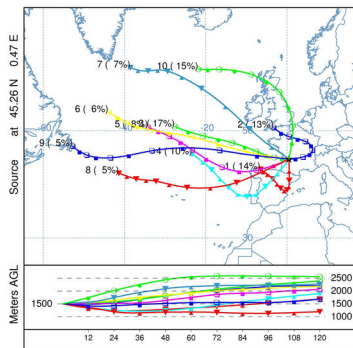
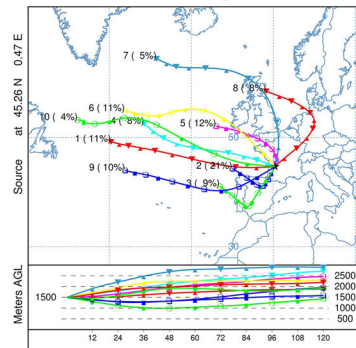
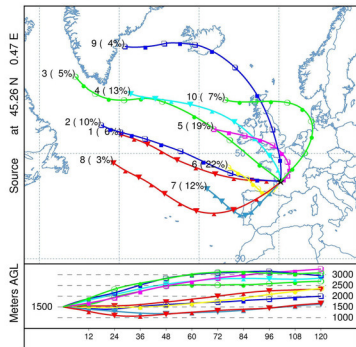
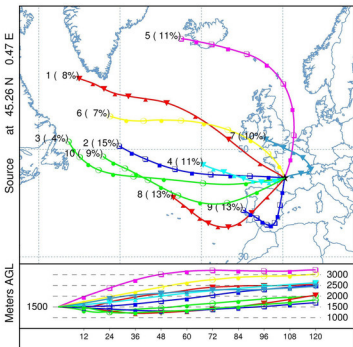
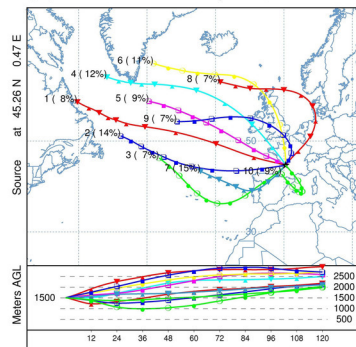
Villars

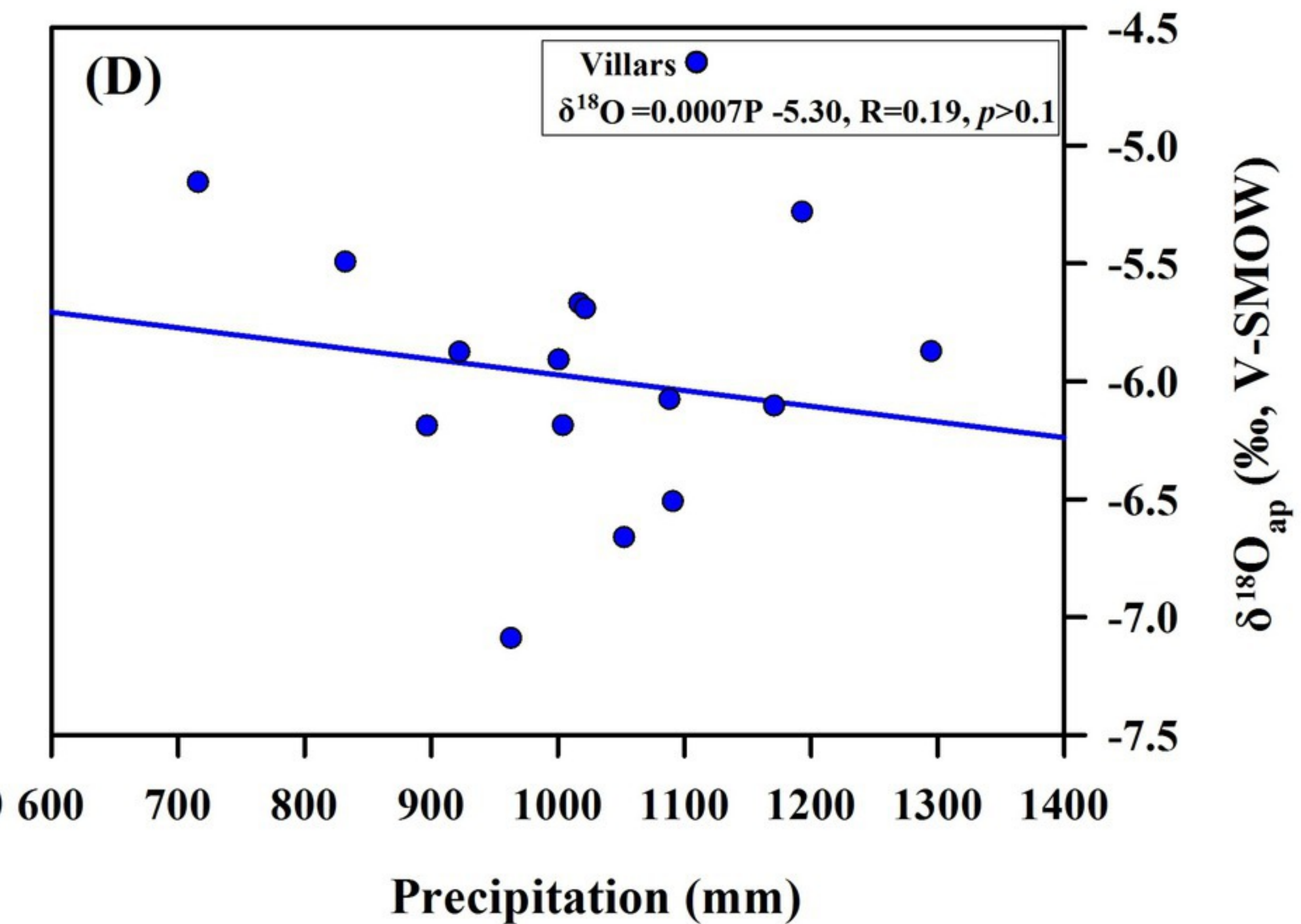
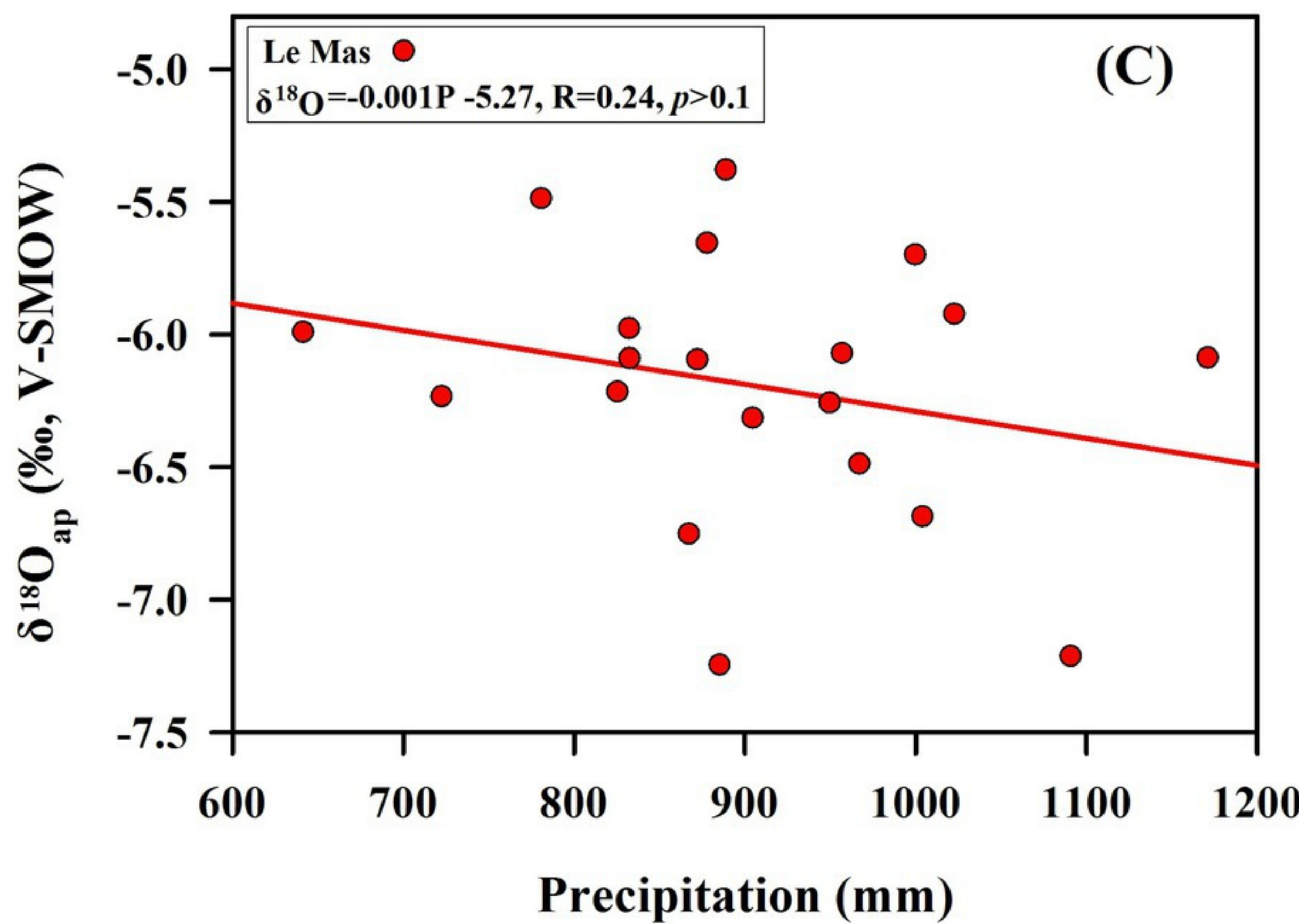
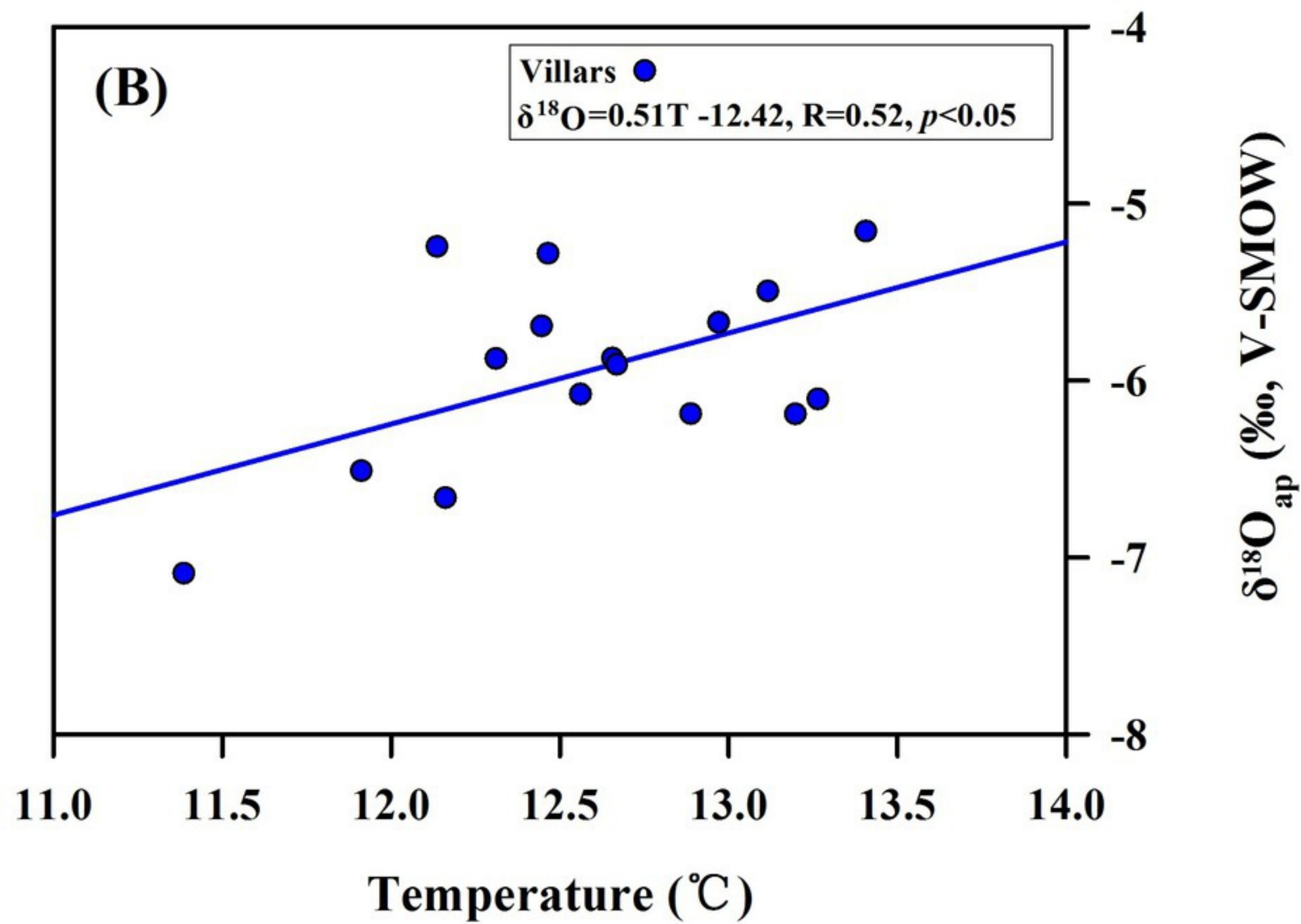
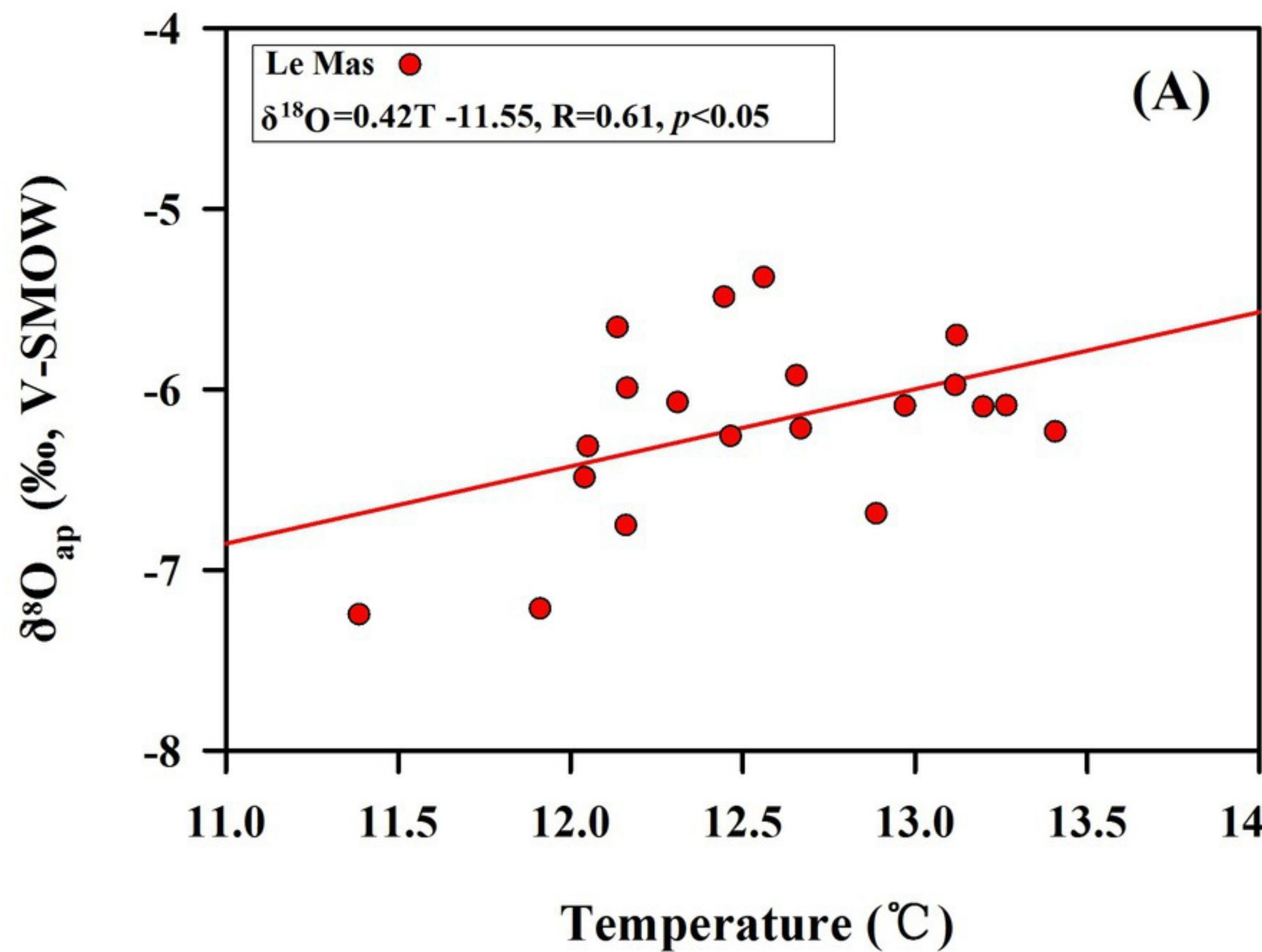


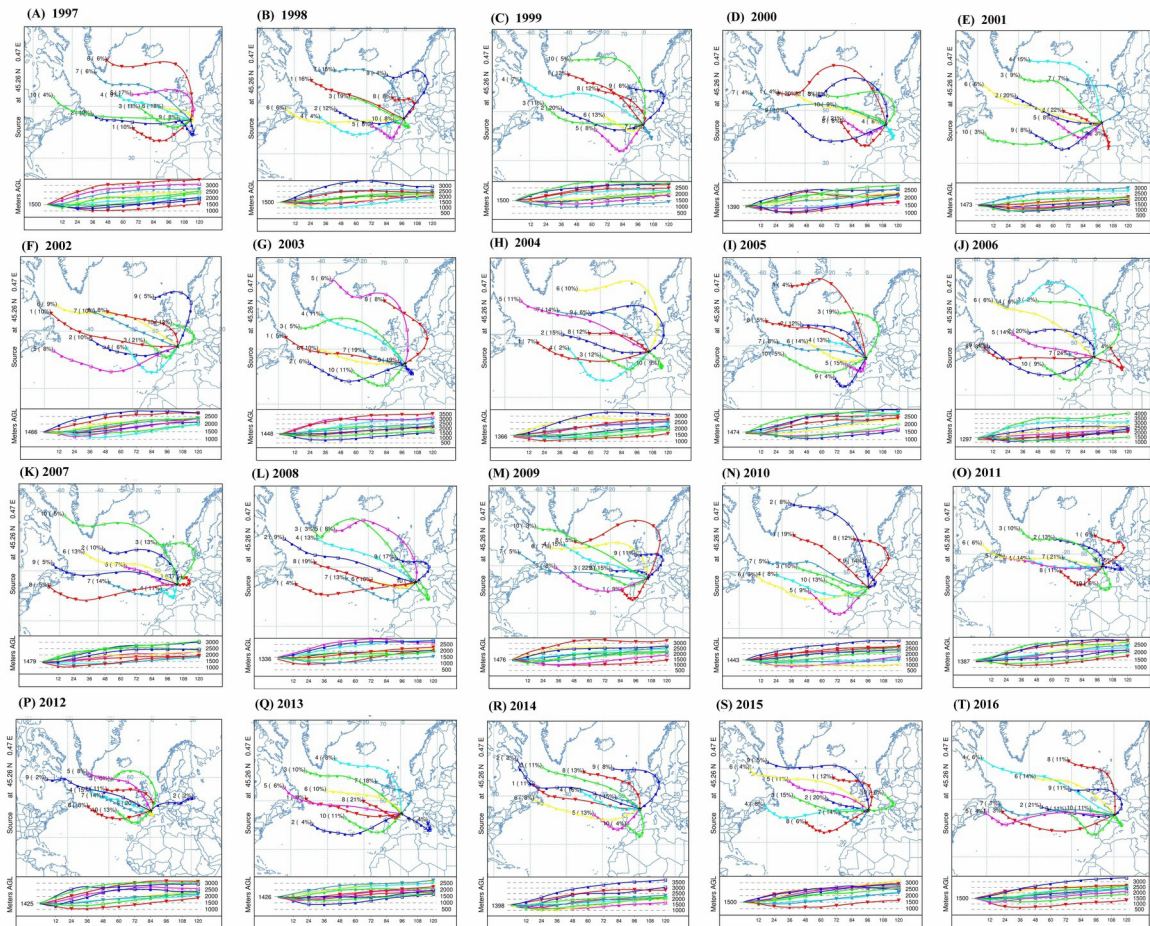


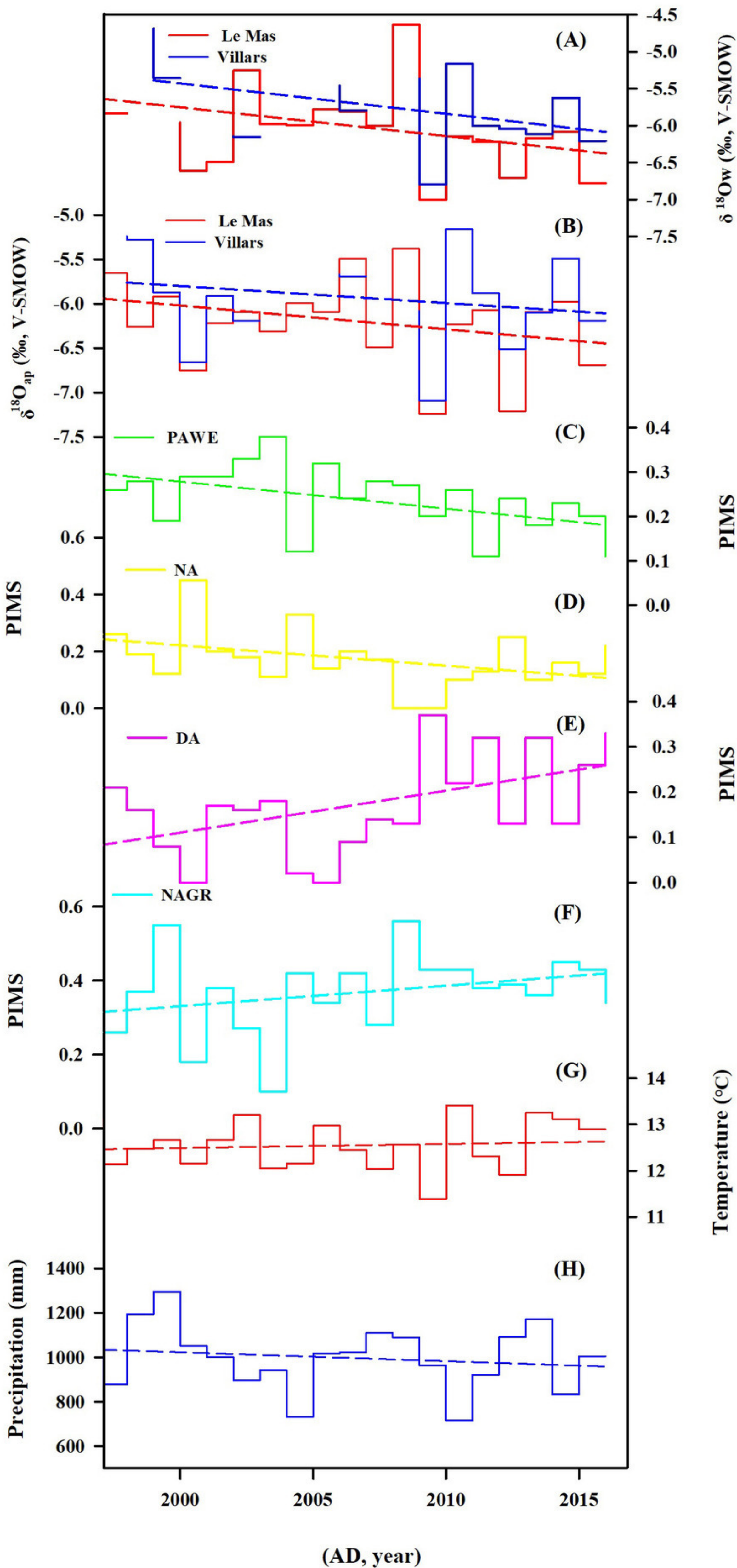


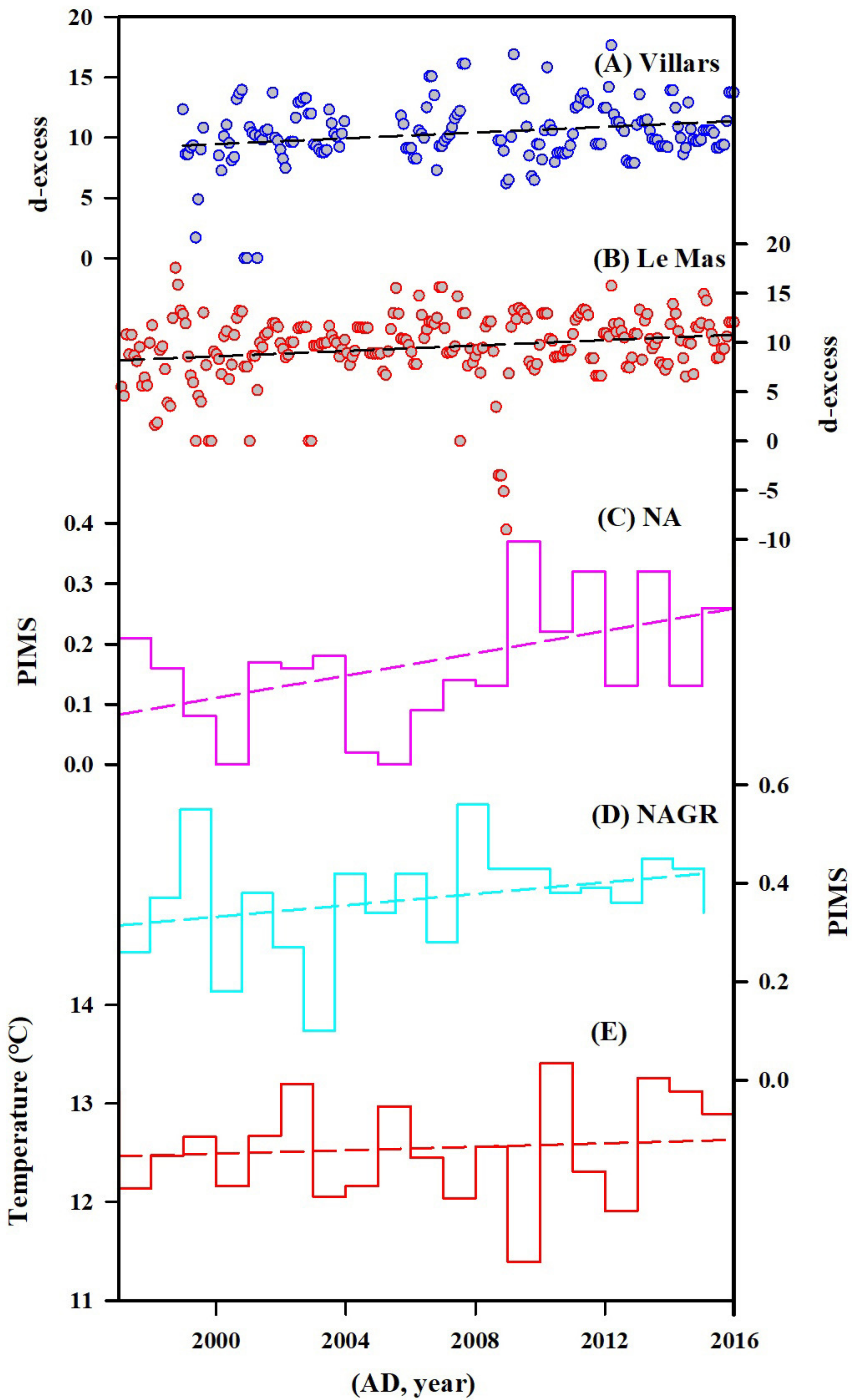
DJF**(A) Dec****(B) Jan****(C) Feb****JJA****(D) Jun****(E) July****(F) Aug**

(A) Mar**MAM****(B) Apr****(C) May****(D) Sep****SON****(E) Oct****(F) Nov**









Tables

Table1 Size by size proximate analysis (as received basis).

Particle size (μm)	Values in (%)				
	Weight	Ash	Moisture	Volatile matter	Fixed carbon
-500+340	14.2	35.4	2.1	21.1	41.5
-340+250	20.1	33.4	2.0	21.4	43.3
-250+180	6.5	30.9	2.2	20.9	46.1
-180+125	16.2	29.3	2.5	20.5	47.8
-125+90	7.9	30.6	2.4	21.1	45.9
-90+75	10.0	36.1	2.3	20.2	41.4
-75+42	19.6	46.7	2.1	20.6	30.7
-42	5.5	50.8	3.2	15.9	30.2
Calculated Head	-	34.7	2.7	20.4	42.3

Table 2 Operating conditions of flotation machine

Operating parameter	Values
Solid concentration during conditioning with reagents, % (w/w)	40
Collector dosage, kg/ton	0.5
Frother dosage, kg/ton	0.25
Agitation time, seconds	300
Conditioning time with collector, seconds	120
Conditioning time with frother, seconds	60
Initial solid concentration for flotation, % (w/w)	10
Froth collection time, seconds	5, 10, 15, 30, 60, 90, 120
pH of the slurry	7.2

Table 3 Performance of three cells for different impeller speeds at different target ash

Impeller Speed: 1200 rpm									
Target Ash%	2 L			4 L			6 L		
	Yield (%)	Time (s)	Com. Recovery (%)	Yield(%)	Time (s)	Com. Recovery(%)	Yield (%)	Time (s)	Com. Recovery(%)
12	-	-	-	-	-	-	9	5	12
13	-	-	-	20	7	29	30	29	41
14	-	-	-	32	22	45	40	120	53
15	-	-	-	50	120	67	-	-	-
16	30	12	39	-	-	-	-	-	-
17	39	40	50	-	-	-	-	-	-
18	45	120	57	-	-	-	-	-	-
Impeller Speed: 1500 rpm									
Target Ash%	2 L			4 L			6 L		
	Yield %	Time (s)	Com. Recovery %	Yield %	Time (s)	Com. Recovery %	Yield %	Time (s)	Com. Recovery %
14	-	-	-	-	-	-	39	29	53
15	-	-	-	29	6	37	47	120	62
16	-	-	-	40	12	51	-	-	-
17	-	-	-	54	60	68	-	-	-
18	27	25	35	-	-	-	-	-	-
19	35	90	44	-	-	-	-	-	-
Impeller Speed: 1800 rpm									
Target	2 L			4 L			6 L		

Ash%	Yield %	Time (s)	Com. Recovery %	Yield %	Time (s)	Com. Recovery %	Yield %	Time (s)	Com. Recovery %
17	-	-	-	-	-	-	54	110	70
18	-	-	-	48	50	63	-	-	-
22	21	12	26	-	-	-	-	-	-
23	31	100	35	-	-	-	-	-	-

Table 4. Ultimate combustible recovery with corresponding rate constants in different cells at different impeller speeds

Parameters	Impeller speed (rpm)								
	1200			1500			1800		
	2 L	4 L	6 L	2 L	4 L	6 L	2 L	4 L	6 L
R_{∞} (%)	57.1±0 .25	71.7±0 .71	61.7±7 .61	48.8±1 .73	72.4±0 .71	61.5±0 .51	38.2±1 .77	68.4±0 .25	70.8±0 .93
ϕ (%)	30.1±1 .19	35.5±0 .75	14.8±5 .01	14.4±1 .56	30.6±3 .18	32.1±2 .27	11.9±2 .86	30.3±1 .42	34.9±8 .14
K_f (s ⁻¹)	0.533± 0.015	0.147± 0.004	0.062± 0.007	0.136± 0.011	0.284± 0.037	0.311± 0.039	0.205± 0.039	0.294± 0.015	0.249± 0.061
K_s (s ⁻¹)	0.039± 0.002	0.017± 0.001	0.004± 0.003	0.016± 0.006	0.036± 0.005	0.043± 0.004	0.023± 0.014	0.046± 0.002	0.051± 0.012
SSE	2.31	0.06	0.32	0.28	0.10	0.46	1.31	0.13	1.80
R^2	1.00	1.00	1.00	1.00	1.00	1.00	0.99	1.00	1.00
Adjusted R^2	0.99	1.00	1.00	1.00	1.00	1.00	0.99	1.00	1.00
RMS E	1.07	0.17	0.40	0.38	0.22	0.48	0.81	0.25	0.95

Table 5 ANOVA derived for yield, ash content, combustible recovery and entrained water recovery models

Statistics	Yield	Ash	Combustible recovery	Entrained water recovery
Sum of squares	594.13	58.07	1118.30	694.01
Degree of freedom	5	2	5	2
Mean square	118.83	29.03	223.66	347
F-value	22.81	47.62	62.82	106.6
p-value	0.0136	0.0002	0.0031	<0.0001
Standard deviation	2.28	0.78	1.89	1.8
R^2	0.97	0.94	0.99	0.97
Adjusted R^2	0.93	0.92	0.97	0.96
Equation	Quadratic	Linear	Quadratic	Linear

Table 6 ANOVA results showing the terms in each response for their respective models

Response	Source	Sum of Squares	Mean Square	F-value	p-value	Remark
Yield	A	2.67	0.53	0.51	0.526	NS
	B	115.19	23.04	22.11	0.0182	S
	AB	217.27	43.45	41.71	0.0075	S
	A ²	2.04	0.41	0.39	0.5758	NS
	B ²	256.96	51.39	49.33	0.0059	S
Ash	A	23.36	11.68	38.32	0.0008	S
	B	34.70	17.35	56.92	0.0003	S
Combustible recovery	A	0.03	0.01	0.01	0.9302	NS
	B	324.14	64.83	91.04	0.0024	S
	AB	354.38	70.88	99.53	0.0021	S
	A ²	2.66	0.53	0.75	0.4509	NS
	B ²	437.09	87.42	122.77	0.0016	S
Entrained water recovery	A	369.58	184.79	113.54	< 0.0001	S
	B	324.43	162.22	99.67	< 0.0001	S
<i>Notes: A: Impeller speed; B: Cell volume; S: Significant; NS: Not significant</i>						